CHEMISTRY OF MATERIALS

Article

pubs.acs.org/cm

Ionic Conduction in Cubic $Na_3TiP_3O_9N$, a Secondary Na-Ion Battery Cathode with Extremely Low Volume Change

Jue Liu,[†] Donghee Chang,[‡] Pamela Whitfield,[§] Yuri Janssen,[†] Xiqian Yu,[∥] Yongning Zhou,[∥] Jianming Bai,[⊥] Jonathan Ko,[#] Kyung-Wan Nam,[∥,♦] Lijun Wu,[○] Yimei Zhu,[○] Mikhail Feygenson,[§] Glenn Amatucci,[#] Anton Van der Ven,[▽,‡] Xiao-Qing Yang,[∥] and Peter Khalifah*[,†,∥]

[†]Department of Chemistry, State University of New York at Stony Brook, Stony Brook, New York 11794-3400, United States

[‡]Department of Materials Science and Engineering, University of Michigan, Ann Arbor, Michigan 48109, United States

[§]Chemical and Engineering Materials Division, Oak Ridge National Laboratory, Oak Ridge, Tennessee 37830, United States

[∥]Department of Chemistry, Brookhaven National Laboratory, Upton, New York 11973, United States

[⊥]Photon Science Division, Brookhaven National Laboratory, Upton, New York 11973, United States

[#]Energy Storage Research Group, Department of Materials Science and Engineering, Rutgers, The State University of New Jersey, 671 US Hwy 1, North Brunswick, New Jersey 08902, United States

[▽]Materials Department, University of California Santa Barbara, Santa Barbara, California 93106, United States

[○]Condensed Matter Physics and Material Science Department, Brookhaven National Laboratory, Upton, New York 11973, United States

Supporting Information

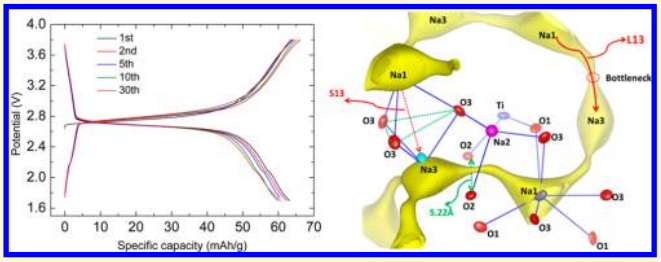

ABSTRACT: It is demonstrated that Na ions are mobile at room temperature in the nitridophosphate compound $Na_3TiP_3O_9N$, with a diffusion pathway that is calculated to be fully three-dimensional and isotropic. When used as a cathode in Na-ion batteries, $Na_3TiP_3O_9N$ has an average voltage of 2.7 V vs Na^+/Na and cycles with good reversibility through a mechanism that appears to be a single solid solution process without any intermediate plateaus. X-ray and neutron diffraction studies as well as first-principles calculations indicate that the volume change that occurs on Na-ion removal is only about 0.5%, a remarkably small volume change given the large ionic radius of Na^+. Rietveld refinements indicate that the Na1 site is selectively depopulated during sodium removal. Furthermore, the refined displacement parameters support theoretical predictions that the lowest energy diffusion pathway incorporates the Na1 and Na3 sites while the Na2 site is relatively inaccessible. The measured room temperature ionic conductivity of $Na_3TiP_3O_9N$ is substantial (4×10^{-7} S/cm), though both the strong temperature dependence of Na-ion thermal parameters and the observed activation energy of 0.54 eV suggest that much higher ionic conductivities can be achieved with minimal heating. Excellent thermal stability is observed for both pristine $Na_3TiP_3O_9N$ and desodiated $Na_2TiP_3O_9N$, suggesting that this phase can serve as a safe Na-ion battery electrode. Moreover, it is expected that further optimization of the general cubic framework of $Na_3TiP_3O_9N$ by chemical substitution will result in thermostable solid state electrolytes with isotropic conductivities that can function at temperatures near or just above room temperature.

1. INTRODUCTION

The rapid growth of the mobile electronic industry has been facilitated by the development of high power Li-ion batteries. The development of next-generation batteries which can meet the demands of the automotive industry and electrical utilities may similarly revolutionize these sectors, though these batteries might not use Li^+ as the mobile ion. The batteries required for these emerging industries are very large and therefore necessitate inexpensive compounds which can still meet desired performance metrics of power, safety, and lifetime. There has therefore been a renewed interest in Na-ion batteries due to the reduced cost and enhanced availability of sodium relative to lithium,[1−3] and depending on the needs of the particular application, the minimum metrics for energy density and rate performance may be relaxed relative to those of the mobile electronics industry.

Some classic Li-ion battery structures have therefore been revisited and tested for their ability to serve as Na-ion batteries. For example, secondary batteries based on the Na-ion analogues of the one-dimensional (1D) Li-ion conductors with the olivine structure ($NaFePO_4$ or $NaFe_{1/2}Mn_{1/2}PO_4$ instead of $LiFePO_4$) have been developed.[4,5] Similarly,

Received: March 30, 2014
Revised: April 27, 2014
Published: April 30, 2014

 © 2014 American Chemical Society

analogues of the very important 2D α-$NaFeO_2$ structure family of $LiCoO_2$ have also been revisited ($NaCrO_2$, $NaVO_2$, $NaNi_{1/3}Mn_{1/3}Co_{1/3}O_2$, etc.) and were found to support reversible Na-ion storage.[6−14] However, good Na-ion analogues of the important 3D cubic spinel class of Li-ion batteries have not yet been found; perhaps the Na-ion battery cathode systems that come closest to achieving isotropic 3D Na-ion conduction are those based on the NASICON structure framework first developed for superionic conduction applications,[15] such as $NaTi_2(PO_4)_3$[16] and $Na_3V_2(PO_4)_3$.[17,18] Although there has been prior work aimed at developing a stable cubic stable framework for isotropic fast Na-ion conduction,[15] this classic goal has not yet been achieved. There have, however, been a number of interesting recent successes in discovering novel structural frameworks with other symmetries which do permit sufficiently rapid room temperature Na-ion conduction to serve as electrode materials for secondary Na-ion batteries, resulting in the development of compounds like $NaVPO_4F$,[19] $Na_3V_2(PO_4)_2F_3$,[20,21] Na_2FePO_4F,[22,23] $Na_3MnPO_4CO_3$,[24] and $Na_2FeSO_4{\cdot}2H_2O$.[25]

In order to expand the range of available structural families capable of transporting mobile ions, we have been motivated to incorporate N^{3-} anions into cathode materials. The use of nitrogen offers potential advantages in energy density since the mass charge ratio of N^{3-} (m/z = 5) is low relative to O^{2-} (m/z = 8) and F^- (m/z = 19), though the detailed structure and stoichiometry of nitrogen-containing compounds will determine whether or not the overall capacity will exceed that of current generation materials. When nitrogen is present in the form of nitridophosphate (PO_3N) groups, inductive effects allow high voltages suitable for cathodes to be realized. We have recently demonstrated that the 2:2 cubic nitridophosphate $Na_2Fe_2P_3O_9N$ can effectively serve as a Li-ion battery at room temperature at voltages above 3 V (vs Li^+/Li) after Li-ion exchange with the theoretical capacity of this compound (144 mAh/g) mostly realized, though higher temperatures (∼300 °C) are necessary to effectively remove Na ions from the framework during the initial ion exchange process due to the low room temperature mobility of Na in this compound. The large difference in mobility between Na and Li in this Fe-containing framework is correctly predicted by bond valence sum (BVS) maps, which give a threshold of more than 0.5 valence units (v.u.) for Na ions, but less than 0.05 v.u. for Li ions.[26] While the room temperature mobility of Na in $Na_2Fe_2P_3O_9N$ is poor, it is worthwhile to ask if higher Na mobilities can be achieved by chemical substitutions in the very intriguing cubic framework of this compound that should be conducive to isotropic Na-ion conduction, and which may be able to effectively serve as a secondary battery cathode or as an isotropic solid state electrolyte, depending on the nature of cation used to replace Fe. In addition to the 2:2 $Na_2M^{II}{}_2P_3O_9N$ compounds with divalent cations, charge balance can also be achieved in 3:1 cubic sodium nitridophosphate compounds with a trivalent cation resulting in the general formula $Na_3M^{III}P_3O_9N$. A variety of redox-active trivalent *3d* transition metals (M = Ti, V, Cr, etc.) can occupy the M^{III} site,[27−32] giving theoretical specific gravimetric capacities of 70−215 mAh/g if one to three Na ions can be cycled electrochemically. The representative $Na_3TiP_3O_9N$ structure is shown in Figure 1.

Our simple bond valence sum map calculations suggest that 3:1 $Na_3TiP_3O_9N$ should have much higher Na-ion mobility than 2:2 $Na_2Fe_2P_3O_9N$. We demonstrate here the validity of this prediction for $Na_3TiP_3O_9N$ through a variety of electrochemical, structural, and theoretical experiments which confirm that there is very good three-dimensional Na-ion mobility at room temperature in this compound. It is shown that $Na_3TiP_3O_9N$ can reversibly cycle Na-ions in a manner suitable for secondary batteries, and that the volume changes on Na-removal are remarkably small (<1%) relative to other known Na-ion battery systems and offer unique advantages toward the development of Na-ion systems with extended lifetimes. Due to the cubic symmetry of this phase, the ionic conductivity of $Na_3TiP_3O_9N$ is fully isotropic unlike other known classes of Na-ions conductors such as beta″-aluminas (two-dimensional Na-ion conductivity)[33] or NASICONs (three-dimensional but anisotropic Na-ion conduction)[15] and may therefore offer unique advantages as a solid state electrolyte. This general class of cubic nitridophosphate structures will be abbreviated as CUBICONs (CUBic Ionic Conductors), in recognition of the Na^+ (and Li^+) ion conduction possible within the framework of these 3:1 and 2:2 nitridophosphate compounds.

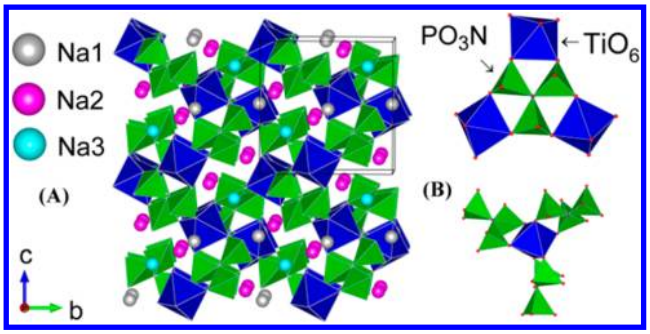

Figure 1. (A) Crystal structure of $Na_3TiP_3O_9N$ viewed along the (100) direction, with unit cell boundaries shown in black. (B) The connectivity of trimers of PO_3N tetrahedra (green) with isolated TiO_6 octahedra (blue).

2. EXPERIMENTAL SECTION

2.1. Synthesis of $Na_3TiP_3O_9N$. For a single-step synthesis of $Na_3TiP_3O_9N$, $NaPO_3$ (Fisher Scientific, $n \sim 6$), and TiO_2 (<32 nm, Alfa Aesar, 99.9%) were combined in a molar ratio of 3.05:1 and ball milled for 120 min in the vibratory ball mill together with 10% (molar ratio relative to Ti^{4+}) ascorbic acid. The mixture was then put into an open-ended fused quartz boat (prepared by cutting open a 15 mm diameter tube) which was then inserted into a 1 in. diameter fused quartz tube and heated at 200 °C/h to a reaction temperature of 850 °C for 20 h under flowing ammonia gas (50 mL/min). A minor (less than 5%) impurity phase of NASICON-type $Na_{3-x}Ti_2(PO_4)_3$ was typically found in the final product when ascorbic acid was not used in the reaction.

2.2. Chemical Desodiation. Powder samples obtained from a single-step solid state synthesis were oxidized with excess 1.0 M NO_2BF_4 in acetonitrile solution for 10 to 20 h in an Ar filled glovebox. The oxidized products were washed with acetonitrile (three times) and then acetone (three times) and were finally dried at room temperature in a glovebox. The color of $Na_3TiP_3O_9N$ powder samples changed from violet to gray after 10 h, indicating the partial oxidation of Ti^{3+}, and then to nearly white after 20 h, indicating a Ti^{4+} valence in the final product which resulted from the very nearly complete sample desodiation.

2.3. Diffraction Studies. Room temperature X-ray diffraction (XRD) data on as-prepared $Na_{3-x}TiP_3O_9N$ powders were collected on a Bruker D8 Advance diffractometer utilizing Cu Kα radiation from a fine focus X-ray tube (Kα1 = 1.54053 Å, Kα2 = 1.54431 Å), with a 300 mm working radius and a 1D position-sensitive LynxEye Si detector with 192 channels. Synchrotron X-ray diffraction data of powder samples were collected at beamline X14A of the National Synchrotron Light Source (NSLS) of Brookhaven National Laboratory (BNL) with

a 1D linear position sensitive detector at a distance of 1433 mm and a wavelength of approximately 0.78 Å. Additional synchrotron XRD data of $Na_{2.5}TiNP_3O_9$ were collected at beamline X7B of the NSLS with a 2D area detector at a distance of 376 mm with a constant wavelength of about 0.32 Å. The software Fit2D[34] was used to convert the 2D diffraction image to a 1D diffraction pattern based on an estimated beam polarization of 90%. *In situ* XRD experiments probing the thermal decomposition of $Na_3TiP_3O_9N$ powders were carried out at beamline X7B. The powder sample was placed in a 1.5 mm quartz capillary, and then the whole capillary was mounted on a thick-wire resistive heater which had been calibrated in advance of the experiment.[35] The sample was heated to 850 °C at 2 °C/min, held at 850 °C for 30 min, and then allowed to naturally cool to room temperature. Structures were refined using the Rietveld method as implemented in the TOPAS software package (Bruker-AXS, version 4.2).

Time-of-flight (TOF) neutron diffraction experiments were performed on the NOMAD[36] and POWGEN powder diffractometers at the Spallation Neutron Source (SNS), Oak Ridge National Laboratory during the 2013-A run cycle (NOMAD) and 2013-B run cycle (POWGEN). For NOMAD experiments, about 100 mg of powder was packed in a 3 mm diameter fused quartz capillary, and typical data acquisition times of 100 min were used. The detectors were calibrated using scattering from the standard diamond powder prior to the measurements. Neutron powder diffraction data were normalized against a V rod, and the background was subtracted using the specific IDL routines developed for NOMAD instrument, including corrections for coherent scattering from the V rod. POWGEN diffraction data were collected with a center neutron wavelength of 1.333 Å. About 1.5 g of sample were loaded into a 6 mm vanadium can which was inserted into a cryofurnace (JANIS) running under a vacuum (pressure less than 10^{-5} bar during data collection). Powder diffraction data were collected with a typical data acquisition time of 3 h. High temperature scans on $Na_3TiP_3O_9N$ were run at temperatures of 300, 400, 500, 595, and 645 K.

The neutron diffraction data were refined using the Rietveld method as implemented in the TOPAS software package (Bruker-AXS, version 4.2). A back-to-back exponential function convoluted with a split pseudo-Voigt function was used to model the peak shape. No absorption correction was needed for the NOMAD data due to the low linear absorption coefficient of both the sample (μ = 0.055 cm^{-1}, μR = 0.0165) and the thin, small diameter capillary. For POWGEN data, a cylindrical absorption correction with estimated absorption coefficient μR ~ 0.35 was used.

2.4. X-Ray Absorption Spectroscopy. X-ray absorption spectroscopy (XAS) data at the Ti K-edge were collected in transmission mode at beamline X19A of the NSLS synchrotron at BNL. Ti metal foil was used as a simultaneous reference energy calibrant. The X-ray absorption near edge structure (XANES) data were processed using the ATHENA software package.[37]

2.5. Electrochemistry. For Na-ion battery testing, electrochemical cycling against a sodium metal anode was done in a 2032-type coin cell. Cathodes were prepared by mixing $Na_3TiP_3O_9N$ powders obtained from the ascorbic acid assisted method for producing a carbon coating during the synthesis procedure (TGA tests indicates about 4 wt% carbon in the powder), carbon black, and PVDF in the mass ratio of 8:1:1. Mixing was done either by hand grinding (all data in main paper) or by low energy milling in a vibratory ball mill (additional data in SI), which led to slightly enhanced electrochemical performance. Coin cells were assembled in an Ar-filled glovebox using thickly cut strips of Na metal as the anode and 1 M $NaClO_4$ in 3:7 (by mass) EC/DMC solution as the electrolyte (***CAUTION!*** *$NaClO_4$ is a strong oxidizer and can react explosively with easily oxidized organics*). The coin cells were tested at room temperature on an Arbin BTU-2000 instrument with a typical current density of 0.014 mA/cm^2 corresponding to a C/20 rate, though other rates were also investigated. Galvanostatic intermittent titration technique (GITT) experiments were carried out on coin cells by first charging for 1 h at a constant current of 0.014 mA/cm^2 and then relaxing for 20 hours and repeating until the potential reached 3.5 V (on charge) or 1.4 V (on the subsequent discharge).

Ionic and electronic conductivities were determined using pellets of $Na_3TiP_3O_9N$ that were synthesized without ascorbic acid (about 12.7 mm in diameter, 1.7 mm in thickness, and 85% dense) prepared by compression under a uniaxial force of 1000 to 4000 kg followed by sintering for 8−16 h at 600 °C under flowing NH_3. Gold contacts (~250 nm thick) were prepared on both sides of the pellet by sputter deposition (Denton Vacuum). The pellet was loaded into a Swagelok-type electrochemical cell, allowing dc polarization data to be collected using Solartron SI1287 and SI1260 instruments. Cells were polarized at 20 mV for 18 h, allowing a sufficient amount of time for ions to be blocked at the gold contacts, a process followed by monitoring the current decay as a function of time. After polarization the cell was left at an open circuit for 12 h, and the voltage decay was used to monitor the relaxation of the cell. Alternating current (ac) impedance measurements were also taken before and after polarization to check for consistency in conductivity calculations and to identify any changes in the cell resulting from polarization. Cells were scanned from 2 MHz to 100 mHz with a 20 mV amplitude sweep. For the activation energy measurements, temperature dependent AC impedance data were collected using a similar pellet of $Na_3TiP_3O_9N$ (about 12.7 mm in diameter/2.5 mm thick) with contacts made by a thick Ag epoxy coating (~1 mm) applied to both faces of the pellet. The pellet was placed on a gold coated glass slide which was then heated on a hot plate. Temperatures at the top and bottom of the pellet were recorded using a thermocouple and averaged, with their temperature difference typically being less than 2 °C. Data was collected both on heating (to 185 °C) and cooling (to 75 °C) using scans from 20 Hz to 2 MHz (5 mV amplitude) on an Agilent E4980A LCR Meter.

2.6. Electron Microscopy. Scanning electron microscope (SEM) images were collected on a JEOL 7600 SEM operating at 5 kV in a low vacuum condition to minimize charging effects. Elemental-dispersive X-ray analysis (EDX) spectra of the as-prepared samples were collected on a JEOL 7600 SEM operating at 15 kV equipped with an Oxford EDX spectrometer. TEM images and electron diffraction patterns were recorded at 300 kV in a JEM-3000F transmission electron microscope equipped with a field emission gun and a Gatan Image Filter spectrometer.

2.7. Thermogravimetric Analysis. Thermogravimetric analysis (TGA) was carried out between 25 and 700 °C on a Q5000IR (TA Instruments) system with a constant flow of oxygen gas (25 mL/min). A 3−4 mg sample was placed on a platinum pan and first stabilized at 50 °C for 2 h to remove moisture potentially present in the powders, then heated to 700 °C at 2 °C/min, held at 700 °C for 4 h, and finally cooled down to 25 °C in a symmetrical manner, allowing overall mass changes to be determined without requiring separate corrections for buoyancy effects when initial and final masses at equal temperatures were compared.

2.8. Bond Valence Sum Maps. Bond valence sum (BVS) maps were calculated using a local computer program incorporating routines from the Crystallographic Fortran Modules Library.[38] In the BVS map calculation, the positions of oxygen and nitrogen were used to calculate the valence of Na within the unit cell using the softBV parameters provided by Adams.[39] Since the soft BVS parameters for N have not yet been determined, the nitrogen was given the same parameters as oxygen ions—a good approximation (hard BVS parameters for N give a valence contribution only 4% different from O at the same distance) that should have negligible influence on the results since the N atoms were far from any potential Li or Na site. The absolute valence difference (ΔV) between the calculated bond valence of Li or Na at each point on a 3D grid within the unit cell and the ideal valence of 1 was then plotted as an isosurface in VESTA.[40] The likely ion diffusion pathways were estimated by increasing ΔV to the minimal values necessary to connect the mobile cation sites into a continuous network. Although there is not a simple relationship between valence and free energy, sites with higher valence differences do represent sites with higher free energies that require higher activation energies to access during diffusional processes. Although the BVS method does not include repulsions from neighboring cations,

this method has been successfully applied to estimate the Li-ion diffusion pathways in $LiFePO_4$ and many other battery materials.[41−44]

2.9. First-Principles Calculations. First-principles calculations were performed using the generalized gradient approximation (GGA-PBE) to density functional theory (DFT) and the Hubbard model extension (GGA+U) as implemented in the Vienna *ab initio* Simulation package (VASP).[45] The effect of the core electrons on the valence states was treated with the projector augmented wave (PAW) method.[46] A plane wave energy cutoff of 600 eV was used. The *k*-point sampling within the Brillouin zone was performed with a 3 × 3 × 3 mesh for the primitive unit cell (containing a total 68 atoms). Equivalent *k*-point densities were used for supercells of the primitive unit cell. All calculations were performed using spin polarization with ferromagnetic ordering of the initial magnetic moments. GGA+U calculations were performed with the method of Dudarev et al.[47] with an effective Coulombic potential of $U_{eff} = U - J$ (effectively, $J = 0$).

It was found that pure GGA calculations with $U = 0$ underestimated the average voltage by more than 1 V, which can be attributed to a large self-interaction error in GGA for localized electronic states. In contrast to simple oxides of Ti like TiO_2, the cubic structure and the isolated Ti octahedra within it are more likely to localize electronic states around Ti. By performing a systematic study of the dependence of the average voltage of the $Na_3TiN(PO_3)_3$−$Na_2TiN(PO_3)_3$ couple relative to a Na metal reference anode on the Hubbard *U* parameter, we determined that a value of $U = 5.0$ eV predicts an average voltage of 2.7 V, which is close to the experimentally measured average voltage. We used this value of *U* to further analyze phase stability and thermodynamic properties at room temperature. The energies of five different Na-vacancy arrangements over the Na1 sites of this structure were calculated within GGA+U. For each Na-vacancy configuration over the Na1 sites, we enumerated all symmetrically distinct Ti^{3+}/Ti^{4+} arrangements and used these to initialize the DFT calculations (by initializing magnetic moments consistent with the particular Ti^{3+}/Ti^{4+} charge ordering). The lowest energy for each of the Na-vacancy configurations was then used to parametrize a cluster expansion[48,49] to describe the variation of the fully relaxed energy with Na-vacancy arrangement. Due to the large distance between neighboring Na1 sites, the cluster expansion Hamiltonian only includes pair, triplet, and quadruplet clusters extending up to the first-nearest neighbor cell. Grand canonical Monte Carlo simulations were applied to the cluster expansion to predict the equilibrium voltage curve (which is related to negative of the Na chemical potential). Migration barriers for Na hops to vacant neighboring sites were calculated with the nudged elastic band method as implemented in VASP using both GGA and GGA+U methods.

3. RESULTS AND DISCUSSION

3.1. Synthesis and Sodium Ion Removal. $Na_3TiP_3O_9N$ powders were prepared by a single-step solid state reaction under flowing ammonia gas similar to the method originally described by Marchand et al.,[27] but with the addition of ascorbic acid to minimize or eliminate the amount of nitrogen-free impurities (typically of the $NaTi_2(PO_4)_3$ NASICON-type structure) that would otherwise form. Rietveld refinements of synchrotron X-ray and time-of-flight (TOF) neutron powder diffraction data confirmed the space group ($P2_13$, #198) and cation stoichiometry (nearly 3:1) expected for this structure type (details in Figure 2 and subsequent figures and tables in the Supporting Information). The structure of this compound consists of TiO_6 octahedra which are linked by trimers of PO_3N tetrahedra that share a central N ion and together form a rigid $[P_3O_9N]^{6-}$ polyanion unit, as can be seen in Figure 1. Potentially mobile Na ions are found within open spaces inside the framework constructed from the TiO_6 octahedra and P_3O_9N tetrahedral trimers. Three different types of sodium sites are present in this structure, with equal abundances but with very different coordination environments despite the fact

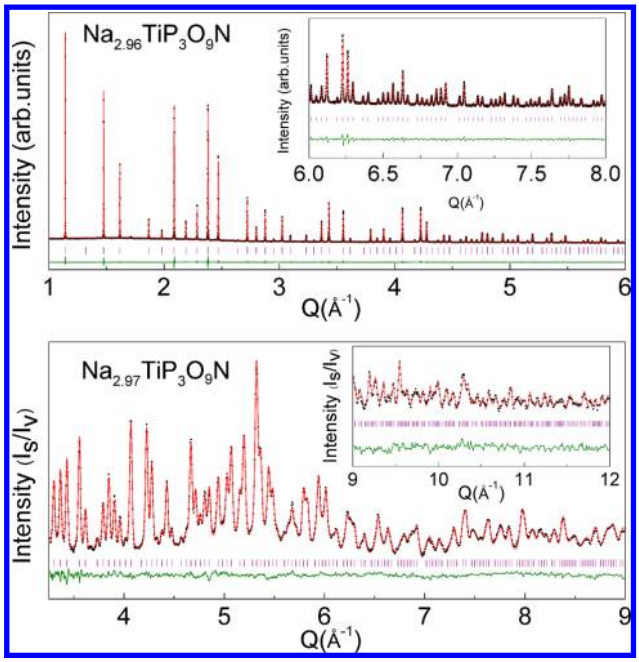

Figure 2. Rietveld refinement of $Na_3TiP_3O_9N$ synchrotron XRD data (λ = 0.7788 Å, top) and TOF neutron diffraction data (2θ = 154° bank, bottom) with experimental data in black dots, calculated pattern in red, tick marks indicating Bragg reflections in purple, and difference curves in green.

that all the Na sites are situated on 3-fold rotation axes. Na1 sits at the center of a NaO_6 trigonal prism, Na2 occupies a distorted octahedron formed by six oxygen atoms, and Na3 is closely coordinated by three oxygens (2.4 Å) with six more oxygen atoms at much longer distances (3.0 and 3.1 Å) that are at best weakly bound. The valences of Na1, Na2, and Na3 were calculated to be 0.67, 1.03, and 0.72, respectively, by hard BVS methods.[50] This suggests that Na ions at Na1 and Na3 sites are weakly bound and should be quite mobile at elevated temperatures if a diffusion pathway exists. This weak bonding was experimentally confirmed by the observation of large sodium thermal displacement values at Na1 and Na3 sites in Rietveld refinements, shown in Figure 2 and discussed in more detail later.

The removal of sodium from this structure and the concomitant oxidation of Ti^{3+} to Ti^{4+} could be chemically driven by reacting $Na_3TiP_3O_9N$ with NO_2BF_4 in acetonitrile. In contrast to $Na_2Fe_2P_3O_9N$ (which requires elevated temperatures of almost 300 °C for the complete removal of Na ions), the essentially complete removal of Na could be accomplished at room temperature in $Na_3TiP_3O_9N$, indicating a large enhancement in Na-ion mobility relative to $Na_2Fe_2P_3O_9N$.[26] The robustness of the $Na_3TiP_3O_9N$ lattice during this process of chemical desodiation is demonstrated by a comparison of the powder XRD patterns of $Na_3TiP_3O_9N$, $Na_{2.5}TiP_3O_9N$, and $Na_2TiP_3O_9N$, which exhibit the same cubic structure before and after Na removal as shown in Figure 3. The (002) peak and (022) peak intensities are particularly sensitive to the changes in Na occupancy. The change in Ti oxidation state during Na-ion removal was reflected both in changes in sample color (violet → gray → white) and in the shifts in the position of the Ti *K*-edge seen in XANES spectra (Figure 3).

The stoichiometry of these $Na_{3-x}TiP_3O_9N$ ($0 \leq x \leq 1$) samples was more precisely investigated through the Rietveld

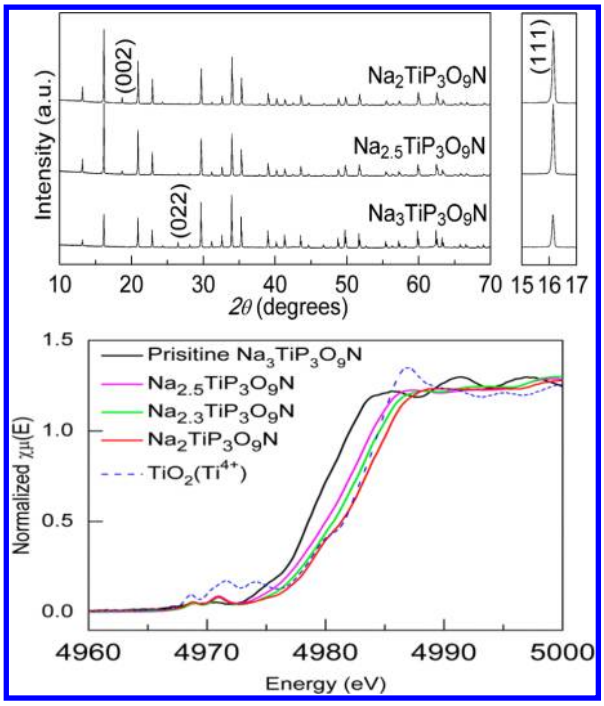

Figure 3. Top: XRD patterns of $Na_{2+x}TiP_3O_9N$ (x = 0, 0.5, 1.0) phases formed by chemical desodiation. Bottom: Ti *K*-edge XANES spectra compared to a Ti^{4+} reference, TiO_2.

refinement of high resolution synchrotron (x = 0, 0.5, 1.0) and time-of-flight neutron (x = 0, 1) diffraction data. The full observed and modeled spectra, data collection parameters, atomic site information, and relevant bond distances are provided in the Supporting Information (Figures S1 to S5, Tables S1 to S7) and will be discussed in more detail when the cycling mechanism of this system is discussed. From these, it is found that the Na1 site is depopulated during the chemical desodiation process. First-principles density functional theory calculations done both within the generalized gradient approximations (GGA) and with a Hubbard model extension (GGA+U) similarly found that Na vacancies are most stable at the Na1 site. Placing the vacancies in the other sodium sites increases the energy by 210 meV (Na2) or 180 meV (Na3) per formula unit, as can be seen in Figure S6.

An intriguing feature of the $Na_{3-x}TiP_3O_9N$ X-ray diffraction patterns is the nearly imperceptible shifts in peak positions during the desodiation process. A Le Bail fitting of laboratory XRD lattice parameters shows a volume change of −0.16% after deintercalation of 0.5 Na and −0.54% after deintercalation of 1.0 Na (Table 1). This cubic Na-ion framework approaches the zero volume change observed for the cubic Li anode spinel, $Li_{4/3}Ti_{5/3}O_4$,[51] a remarkable result given that Na ions have an ionic volume about 150% larger than Li ions (4.4 vs 2.4 Å^3). The observed small volume changes are in good agreement with theory as GGA+U calculations predict a volume change of −0.6% upon removal of Na from $Na_3TiP_3O_9N$ to form $Na_2TiP_3O_9N$ (Figure S6). Since the cycling-induced development of stresses and subsequent cracking can be a major failure mechanism in systems with large volumetric changes, it is expected that the present system could be very suitable for extended cycling applications if other failure mechanisms (*i.e.* those associated with surface reactions) in the electrochemical cell can be identified and eliminated. Small volume changes are also very desirable for all solid state batteries, which would further benefit from the isotropic nature of this structure type.

Table 1. Volume Changes on Desodiation of $Na_3TiNP_3O_9N$

compound	a (Å)	V (Å^3)	ΔV
$Na_{2.96}TiP_3O_9N$	9.5219(1)	863.33(1)	
$Na_{2.47}TiP_3O_9N$	9.5170(3)	861.98(7)	−0.16%
$Na_{2.08}TiP_3O_9N$	9.5048(1)	858.69(1)	−0.54%

3.2. $Na_3TiP_3O_9N$ As a Na-Ion Battery Cathode. The complete oxidation of $Na_3TiP_3O_9N$ during chemical desodiation and the extremely small volume change of the open cubic framework of this phase during this process indicate that $Na_3TiP_3O_9N$ may be an excellent electrode material for Na-ion batteries. Indeed, it was determined that $Na_3TiP_3O_9N$ can be very effectively cycled against a Na metal electrode using an electrolyte of 1 M $NaClO_4$ in 3:7 EC/DMC with a promising Na-ion rate performance and reversibility with an average voltage of about 2.7 V vs Na^+/Na, as shown in Figure 4. At a charge/discharge rate of C/20, a discharge capacity of 67 mAh/g (91% of the theoretical capacity of 74 mAh/g) is achieved in the first cycle, with discharge capacities stabilizing at 50−60 mAh/g over the subsequent 50 cycles, depending on the charging rate. Unlike many other Na-ion systems, no intermediate plateaus are observed during charge/discharge. This is likely a consequence of the worm-like diffusion channels within this material, which lead to a higher degree of screening of Na^+ ions from each other, thus inhibiting the formation of Coulombically stabilized intermediate phases with different types of Na-ion ordering during charge/discharge cycles. While relatively small polarization was observed in the middle of the charge/discharge curves, higher polarization was observed near the ends of these curves. This is attributed to kinetic limitations in accessing the center of particles due to limitations in the time scale of ionic or electronic conduction. This assignment is confirmed by GITT experiments, which clearly demonstrate that the system relaxes to voltages close to the average potential when the system is allowed to fully equilibrate.

This is also consistent with the reduction in accessible capacity when the cycling rate is increased from C/40 to C/5. The typical particle size of $Na_3TiP_3O_9N$ observed in SEM experiments (Figure 5) and TEM experiments (Figure S7) was on the order of 1−5 μm in diameter and 0.5 μm in the minimum dimension, suggesting that there is an opportunity to improve the electrochemical performance of this system if improved syntheses which reduce the particle size can be developed. The presence of facets on these particles suggests that partial melting of precursors may occur during the synthesis, and that smaller particle sizes cannot be achieved without switching to precursors (or reaction conditions) that promote higher melting point. Initial efforts to reduce the particle size using a vibratory mill resulted in improved capacity retention, though XANES spectra indicated that some oxidation was found to occur when this milling was carried out under an air atmosphere (Figures S8, S9).

Since no evidence of a plateau is seen in the GITT data, it is concluded that the cycling occurs through a solid solution rather than a two-phase mechanism. The mechanism can be further explored through density functional theory. The voltage profile of $Na_3TiP_3O_9N$ was calculated from Monte Carlo simulations performed on a cluster expansion Hamiltonian describing the energy of Na-vacancy disorder parametrized by GGA+U total energy calculations. At 0 K, GGA+U calculations

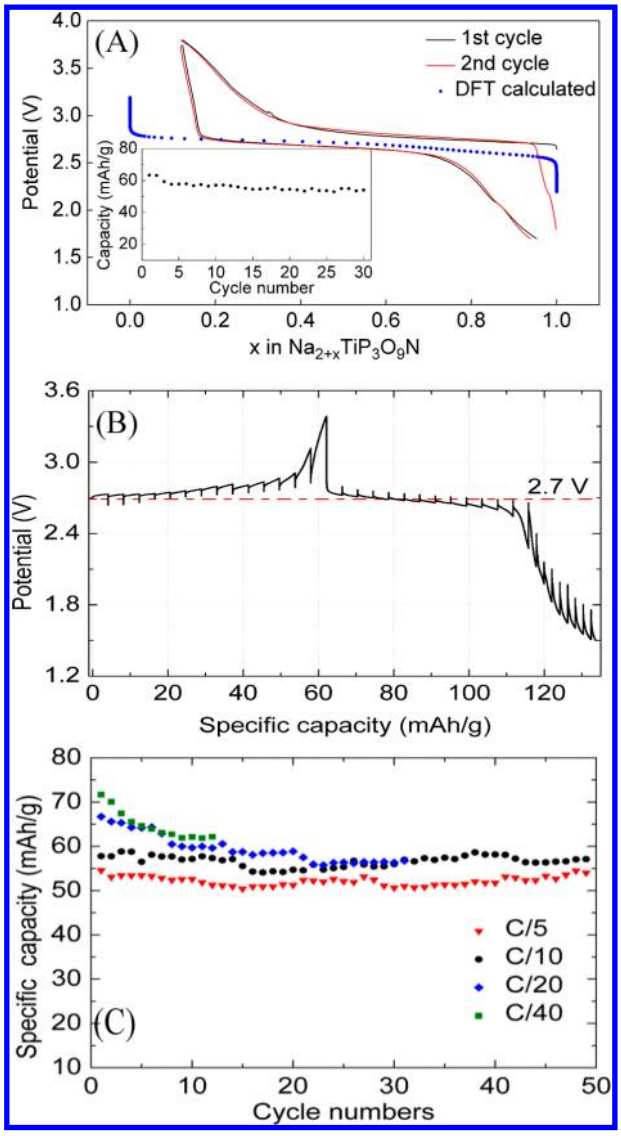

Figure 4. . (A) Electrochemical performance of $Na_3TiP_3O_9N$ cathodes cycled against Na metal. The voltage (vs Na^+/Na) charge−discharge curve of $Na_3TiP_3O_9N$ was obtained at C/20. The thermodynamic charge−discharge curve predicted by DFT calculation is overlaid (blue dotted symbols). (B) GITT curve of $Na_3TiP_3O_9N$ cathode cycled against Na metal. (C) Capacity retention of $Na_3TiP_3O_9N$ cathode cycled against Na metal.

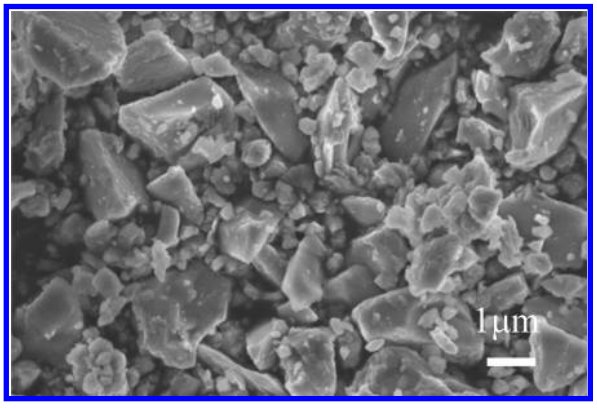

Figure 5. SEM image of $Na_3TiP_3O_9N$ particles. Scale bar is 1 μm in length.

predict that that there will be ordering of the Na vacancies (on Na1 sites) in partially desodiated samples resulting in a two-phase reaction mechanism at this temperature. However, this vacancy ordered structure has only slightly positive formation energies relative to $Na_2TiP_3O_9N$ and $Na_3TiP_3O_9N$, and as a result, Monte Carlo simulations predict that solid-solution behavior with a slightly sloping voltage profile should be seen at room temperature (blue dots, Figure 4A), behavior which is indeed observed in experimental GITT measurements.

3.3. Ionic Conductivity Studies. The facile chemical desodiation and reversible electrochemical cycling of $Na_3TiP_3O_9N$ suggests that the ionic conductivity within this structural framework may be good. The possibility of achieving high Na^+ ion conductivity within an isotropic cubic framework is especially intriguing, as there are not many existing materials with this combination of properties, though some promising oxide and oxoanion cubic frameworks have previously been screened for this purpose.[15] The Na^+ mobility within the $Na_3TiP_3O_9N$ CUBICON structure was first studied by dc polarization measurements on sintered pellets (∼85% dense) of $Na_3TiP_3O_9N$ with gold blocking electrodes (Figure 6). The current decayed by more than 98% after relaxation, indicating that the ionic conductivity ($\sigma_I = 4.2 \times 10^{-7}$ S/cm) of pristine $Na_3TiP_3O_9N$ far exceeds its electronic conductivity ($\sigma_e = 6.8 \times 10^{-9}$ S/cm) at room temperature. This ionic conductivity is quite substantial, and it is likely that the framework ionic conductivity can be enhanced considerably by the intentional introduction of Na vacancies, or by substitutions on the transition metal site. The electronic conductivity for this compound is somewhat low in a manner reminiscent of phosphate battery electrode materials. During cycling, the electrical conductivity is expected to somewhat increase relative to the integer valence pristine material but will likely remain the limiting factor for cycling rates due to the lack of direct metal−oxygen−metal linkages between transition metal sites.

Further insights into the ionic conductivity of $Na_3TiP_3O_9N$ were obtained from ac impedance measurements (Figure 6). The data at all temperatures were well modeled using an equivalent circuit previously proposed for solids with primarily ionic conductivity (ref 52) and represent an upper limit for the bulk conductivity since the actual sample contains abundant grain boundaries which may also contributed to the overall conductivity. The fit process is described in more detail in the Supporting Information (Figure S10). The temperature dependence of conductivity followed a modified Arrhenius form of $\sigma T = \sigma_0 \exp(-E_a/k_B T)$ with an activation energy of 0.54 eV (52 kJ/mol). The total conductivity was found to be 2.5×10^{-7} S/cm at 30 °C and 4.0×10^{-5} S/cm at 163 °C. This conductivity is similar to that observed for some NASICON-type $NaM_2(PO_4)_3$ compounds,[53] though it is about 2 orders of magnitude lower than for fully optimized NASICON $Na_3Zr_2PSi_2O_{12}$.[15] It is expected that the conductivity of the CUBICON framework can be similarly optimized by substitution (aliovalent doping to increase the vacancy content, or isovalent doping to tune the size of the diffusion channels). Furthermore, our prior studies on $Li_xFe_2P_3O_9N$ found that Li is substantially more mobile than Na within this framework,[26] suggesting that Li conductivity in the CUBICON framework may be increased by a few orders of magnitude and might potentially permit the observation of Li superionic conduction.

Good insights into the potential wells associated with the three sodium sites in $Na_3TiP_3O_9N$ can be gained from the displacement parameters refined using high resolution time-of-

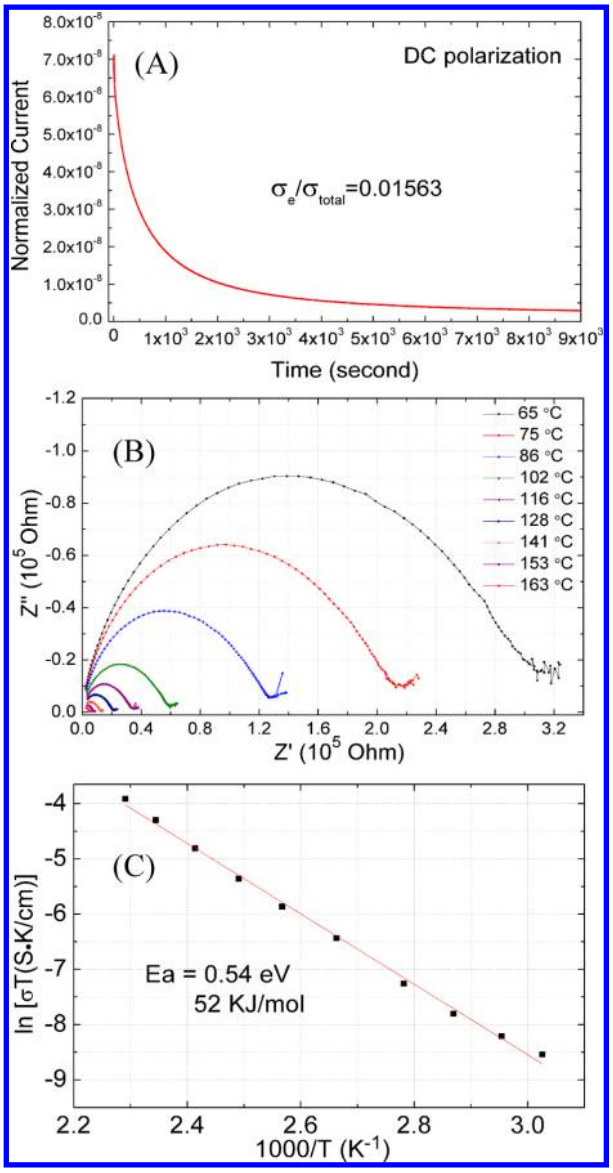

Figure 6. (A) Decay of dc current for $Na_3TiP_3O_9N$ polarized at 20 mV. (B) $Na_3TiP_3O_9N$ ac impedance spectra and (C) the Arrhenius behavior of the derived activation energy.

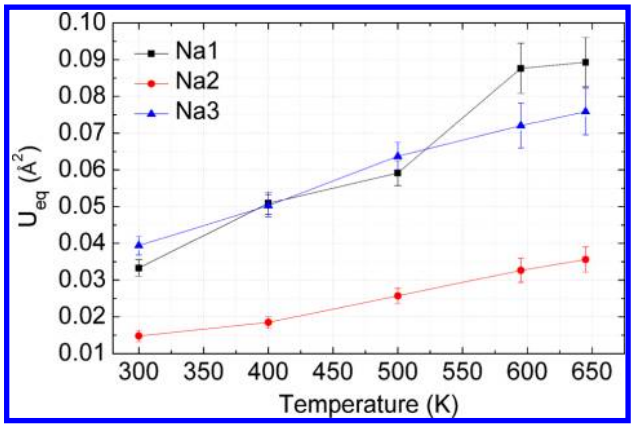

Figure 7. Temperature-dependent displacement parameters for the sodium sites of $Na_3TiP_3O_9N$ from neutron diffraction data.

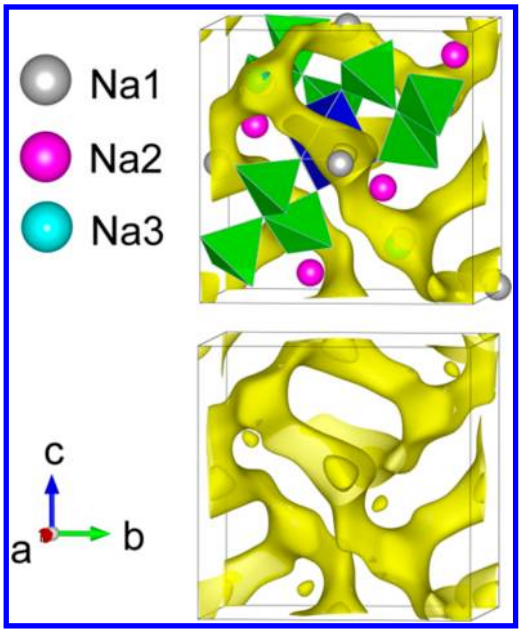

Figure 8. Na difference bond valence sum ($|\Delta V|$) map of $Na_3TiP_3O_9N$ (top) and $Na_2TiP_3O_9N$ (bottom) drawn with an isosurface level of 0.12. The Na1 and Na3 sites (white and blue spheres, respectively) are predicted to be part of a three-dimensional ion conduction network, while the Na2 sites (purple) are expected to be isolated from this network.

flight neutron diffraction data (d_{min} ~ 0.3 Å) acquired on the POWGEN diffractometer. The very large room temperature displacement parameters refined for Na1 (U_{eq} = 0.033 Å^2) and Na3 (0.039 Å^2) far exceed that of Na2 (0.015 Å^2) and the other nonsodium atoms (Figure 7). These displacements are strongly enhanced by increasing temperature, confirming that they represent dynamic rather than static displacements. The average displacement inferred from these parameters increases from about 0.2 Å at room temperature to 0.3 Å at 650 K. This indicates that Na1 and Na3 have very shallow potential wells which are conducive to fast ionic diffusion if a suitable diffusion pathway exists.

In order to visualize possible diffusion paths for Na ions within this structure type, bond valence sum (BVS) difference maps[54] were calculated. It is expected that all positions within the cell where the absolute value of the valence difference ($|\Delta V|$) between the BVS-calculated valence and the ideal valence of +1 is small represent low free energy positions that are accessible to Na at modest activation energies. The likely diffusion paths of Na ions are represented by the $|\Delta V|$ isosurfaces shown in Figure 8, which were calculated based on the refined structures for stoichiometric $Na_3TiP_3O_9N$ (top) and desodiated $Na_2TiP_3O_9N$ (bottom). The Na1 and Na3 sites of $Na_3TiP_3O_9N$ first become connected in a continuous network when a very small $|\Delta V|$ threshold of 0.03 is chosen, and Na ions at these two sites are therefore predicted to be mobile and to form an isotropic three-dimensional ion transport network. The Na2 site requires a much larger threshold of 0.45 valence units to be connected, and it is therefore expected to be difficult to access these sites at room temperature. A comparison of threshold $|\Delta V|$ values for network formation of $Na_{3-x}TiP_3O_9N$ structures determined in this work (Table 2) suggests that similar behavior will be observed for structures with different sodium concentrations, though the barrier for accessing Na2 is lowered when Na is partially or fully removed. The relative barriers to diffusion predicted for the three Na sites are very

Table 2. Threshold Values for Sodium Bond Valence Difference (|ΔV|) Map

linkage type	$Na_3TiP_3O_9N$	$Na_{2.5}TiP_3O_9N$	$Na_2TiP_3O_9N$
Na1−Na3	0.03	0.02	0.05
Na1−Na2−Na3	0.45	0.24	0.29

consistent with the displacement parameters associated with these sights, suggesting that the primary barrier to motion in the diffusional process is directly associated with the potential well in the immediate vicinity of the Na atoms.

Although BVS maps have been found to be a convenient and effective method to visualize possible diffusion pathways, they do not include cation−cation repulsions and only qualitatively correspond to the potential energy surface associated with the mobile ions. Careful crystal structure analysis of the local environments of the sodium ions may provide further insights into the possible diffusion paths. From the refined crystal structure of $Na_3TiP_3O_9N$, it can be seen that the shortest direct paths between two Na1 sites or two Na3 sites are forbidden due to the presence of intervening TiO_6 octahedra and PO_3N tetrahedra, consistent with the BVS predictions. The most likely diffusion pathways instead involve heterogeneous migration paths in which ions consecutively access both Na1 and Na3 sites. Two possible paths of this type through open space have been identified and will be referred to as S13 and L13 for the shorter (3.44 Å) and longer path (4.44 Å), respectively. As seen in Figure 9, the S13 path involves migration through an equilateral triangle formed by three O3 atoms (with O3−O3 bond lengths of 3.10 Å) which are part of the coordination sphere of both Na1 and Na3. The S13 path is located directly on the 3-fold axis on which both the Na1 and Na3 sites are found. In contrast, the L13 path radiates away from each site in three different directions since it is not collinear with a 3-fold symmetry axis. This path allows Na ions to pass through a much more open triangle formed by two O1 ions associated with the Na1 coordination shell and one O3 ion that is part of the Na2 octahedral environment.

While BVS maps provide a rapid method for identifying potential diffusion paths, DFT calculations are better able to quantify hopping energies and are more directly comparable with experimental results. In order to understand the diffusion process, it is necessary to understand which sites have kinetically accessible hopping pathways, and which sites have an occupancy that varies with the state of charge (only the Na1 site of $Na_3TiP_3O_9N$). It is interesting to note that the desodiation of 2:2 $Na_2Fe_2P_3O_9N$ removes twice as many Na ions per formula unit,[26] and that these two Na ions are removed from sites which correspond to the Na1 and Na3 sites of $Na_3TiP_3O_9N$, supporting the BVS prediction that the diffusion path connects Na1 and Na3 sites. First-principles density functional theory calculations done within both the generalized gradient approximations (GGA) and the Hubbard model extension (GGA+*U*) also indicate a fully three-dimensional diffusion path that links both Na1 and Na3 but not Na2 sites.

The energy barriers of three possible diffusion pathways (illustrated in Figure 10) were calculated by DFT+U methods upon introduction of one Na vacancy in the 68 atom primitive cell. The lowest energy pathway was found to be along the L13 path from Na1 to Na3. As Na migrates along the long paths, it will pass through an intermediate local minimum where it is likely to thermalize before hopping further into either the Na1 or Na3 sites. This local minimum coincides with a 4-fold oxygen coordinated site, similar to the intermediate tetrahedral sites of Li hops in many Li intercalation compounds.[55] The topology of the structure is such that the long path (L13) will allow fully isotropic three-dimensional diffusion. Two barriers of 0.5 and 0.29 eV need to be overcome when migrating from the Na3 site to the Na1 site. In the opposite direction, the Na will experience a barrier of 0.37 eV followed by a very small barrier of less than 0.10 eV.

Although the net energy barrier of 0.75 eV for moving from Na3 to Na1 is higher than the experimentally measured activation energy of 0.54 eV, the possibility of a stable intermediate would lower the theoretical barrier to only 0.50 eV, a value in good agreement with experimental results. The simple GGA energy profile obtained without the inclusion of a Hubbard U shows a similar total energy barrier (0.62 eV) but does not exhibit a well-resolved intermediate site (Figure S11). The complexity of the energy landscape connecting Na1 and Na3 sites makes it uncertain that the total migration barrier from Na1 to Na3 can simply be equated to an average activation barrier obtained experimentally. Further kinetic Monte Carlo simulations will be needed to better determine the equivalent average migration barrier for a complex energy landscape with many distinct hop types having a spectrum of migration barriers. Intriguingly, the potential energy landscape

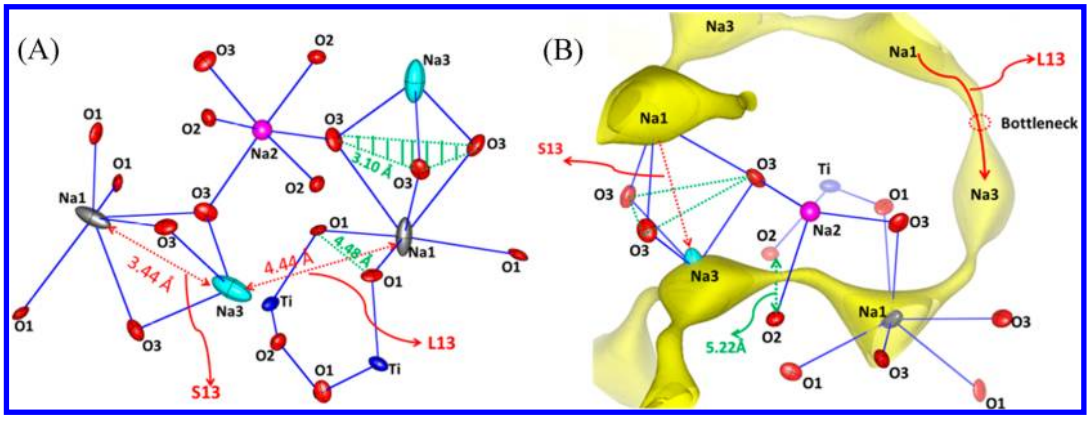

Figure 9. (A) Thermal ellipsoids (50% probability) of ions near the two most plausible sodium ionic diffusion paths (S13 and L13) in $Na_3TiP_3O_9N$. (B) Plot of the Na difference bond valence map (|ΔV| = 0.05) suggests that the barrier for moving between the Na1 and Na3 sites is low along the longer L13 type path but is high along the S13 type path (remains disconnected even for |ΔV| = 0.5) .

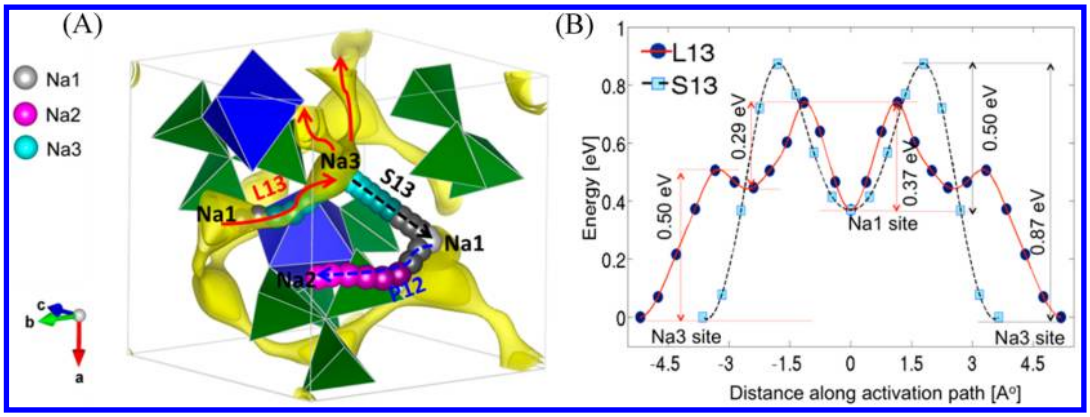

Figure 10. (A) Visualization of the three potential diffusion paths evaluated using DFT+U calculations, superimposed on the BVS map ((|Δ*V*| = 0.05, yellow) . The favored L13 path (red, 0.50/0.37 eV) is marked with a solid red arrow, while dashed lines indicate the high barrier pathways S13 (black, 0.87/0.50 eV) and P12 (blue, 0.98/0.75 eV). (B) DFT+U energies for points along the short (S13) and long (L13) Na1−Na3 pathways, with energies evaluated at positions marked by spheres in the left panel.

suggests that the overall diffusional barrier could potentially be further lowered if the Na3 site is destabilized through chemical substitutions (at the sites of nonmobile ions), as a major contributor L13 diffusional barrier is the difference in Na potential energy between the Na1 and Na3 sites.

Although a shorter S13 diffusion path between the Na1 and Na3 sites is nominally available, the limiting barrier for this pathway is calculated to be 0.87 eV for Na3 → Na1 hops. Due to the difference in the Na1 and Na3 site energies, a lower barrier of 0.47 is predicted for Na3 → Na1 hops, though this lower barrier is not the limiting one for diffusion through the network of Na1 and Na3 sites. In contrast to the L13 hop, the S13 barrier shows no evidence of an intermediate resting site and clearly must be overcome in a single hop. The high barrier of 0.87 eV for the S13 path suggests that this pathway is unlikely to be important to ion diffusion in $Na_3TiP_3O_9N$. A similar energy barrier (0.89/0.57 eV) is found for the lowest energy path for Na migration between the Na1 and Na2 sites, denoted P12. While this barrier is too large for the Na2 site to significantly contribute to the overall ionic mobility of $Na_3TiP_3O_9N$ at room temperature, it is not expected to be large enough to prevent site exchange at the Na2 site at elevated temperatures. This is experimentally confirmed by our Li ion-exchange studies, which will be described elsewhere.[56]

3.4. Thermal Stability of $Na_3TiP_3O_9N$ Framework. The safety of battery systems is of significant concern for portable electronics applications, and may become even more important in applications which utilize larger battery systems (electric vehicles, grid-scale storage). The thermal stability of cathode materials has been shown to be a good predictor of stability against overcharge.[57] Although nitride and oxynitride systems can be susceptible to decomposition by oxygen attack, some systems like GaN or SIALONs have very good temperature stability to ∼900 °C.[58,59] Furthermore, nitridophosphate systems have the potential for the loss of inert N_2 rather than reactive O_2 loss, potentially mitigating their reactivity with organic electrolytes. Finally, the fully charged state of $Na_3TiP_3O_9N$ contains Ti^{4+}, an oxidation state which is very resistant to oxygen loss (in sharp contrast to tetravalent *3d* transition metals such as Mn, Fe, or Co, which are typically susceptible to oxygen loss). Thermogravimetric analyses (TGA) were used to assess the thermal stability of $Na_3TiP_3O_9N$ by following the mass changes that occurred on heating in an O_2 atmosphere (Figure 11). Full decomposition

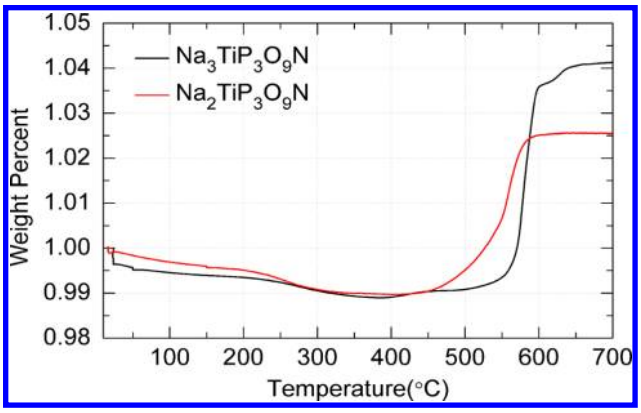

Figure 11. Thermogravimetric response of pristine $Na_3TiP_3O_9N$ (black) and chemically desodiated $Na_2TiP_3O_9N$ (red) on heating (2 °C/min, flowing O_2) .

did not occur until temperatures in excess of 550 °C. The onset of mass gain begins above 400 °C, although it is not clear if initial mass loss is due to framework decomposition (1.5 O^{2-} ions replace each N^{3-}) or Ti oxidation (Ti^{3+} oxidized to Ti^{4+} charge balanced by the gain of 0.5 O^{2-}) as both of these processes involve mass gains. In either case, this mixed anion compound can be considered to have good oxidative stability in a manner analogous to $LiFePO_4$, which thermally decomposes around 550 °C.[60] When $Na_3TiP_3O_9N$ is fully desodiated to produce $Na_2TiP_3O_9N$ using a chemical oxidant, this framework still remains stable against oxidation in O_2 up to at least 400 °C.

In order to get a more direct measure of the framework stability and the decomposition processes, *in situ* X-ray diffraction data (Figure 12) were collected at the X7B beamline of the NSLS synchrotron. Up to 550 °C, the only crystalline phase is $Na_3TiP_3O_9N$. At 575 °C, peaks appear for a second crystalline phase which can be indexed based on the NASICON-type phase $NaTi_2(PO_4)_3$. Rietveld refinement of the last diffraction pattern collected at 200 °C (Figure S12) showed this phase crystallized in space group of $R\bar{3}c$ with lattice parameters of a = 8.4736(3) and b = 21.9502(10). These results are consistent with our synthetic studies, which also show this NASICON phase as a common impurity which cannot be converted to $Na_3TiP_3O_9N$ by any amount of annealing under NH_3, suggesting that this is an irreversible transformation driven by nitrogen loss. The transformation of

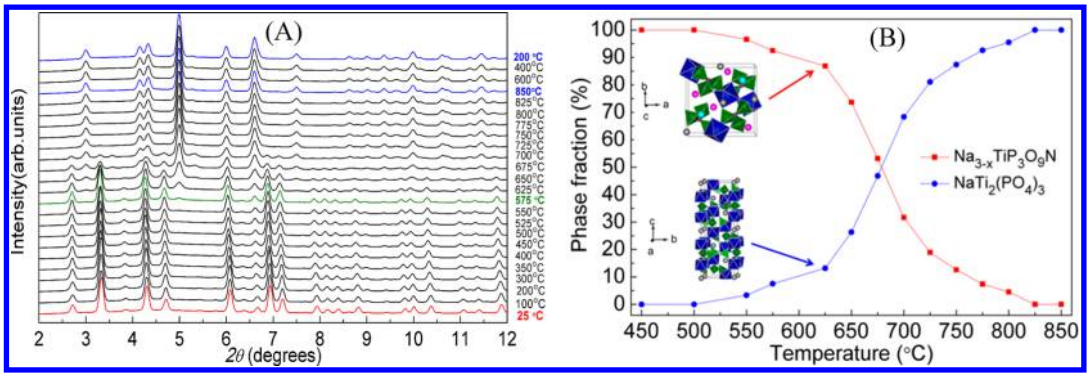

Figure 12. (A) *In situ* XRD data (λ = 0.3196 Å) following the transformation of CUBICON $Na_3TiP_3O_9N$ heated under flowing air. Thermal decomposition was first observed at 575 °C, and the only decomposed product giving diffraction peaks could be indexed as NASICON-type $NaTi_2(PO_4)_3$. (B) Refined phase fractions of CUBICON and NASICON components.

$Na_3TiP_3O_9N$ to $NaTi_2(PO_4)_3$ was observed to be complete by 725 °C, suggesting that this reaction occurs quickly in the present of oxygen.

4. CONCLUSIONS

In conclusion, $Na_3TiP_3O_9N$ is shown to be the first member of the CUBICON family of nitridophosphate compounds that can effectively cycle Na ions reversibly at room temperature. The 3D Na-ion conduction pathways, good sodium ionic conductivity, extremely small volume changes, high redox potential (0.6 V higher than equivalent Ti^{4+}/Ti^{3+} redox couple of NASICON-type $Na_3Ti_2(PO_4)_3$ cathodes), and good thermal stability make this structure type particularly attractive for rechargeable Na-ion battery applications. Although the capacity of $Na_3TiP_3O_9N$ is somewhat limited (74 mAh/g) for practical cathode applications, this CUBICON framework contains two readily mobile Na ions (and three Na ions in total) per transition metal site, so the theoretical capacity of this framework can be doubled or even tripled if transition metals such as V^{3+} (V^{4+}, V^{5+}) or Cr^{3+} (Cr^{4+}, Cr^{5+}, Cr^{6+}) that can access more than two oxidation states are substituted for Ti^{3+}. Also, significantly higher voltages are expected when other trivalent transition metals are substituted for Ti^{3+}. In general, the Li-ion variants of the CUBICON framework appear to have substantially higher ionic conductivities than their Na-ion analogues, and appropriate chemical substitutions may offer the possibility of discovering superionic conductivity within this isotropic cubic framework—ideal behavior for a solid state electrolyte.

■ ASSOCIATED CONTENT

Supporting Information

Fits and structures obtained from Rietveld refinements, DFT site energies, SEM and TEM results, XANES measurements, additional cycling data, EIS fitting, Rietveld analysis of thermal decomposition product. This material is available free of charge via the Internet at http://pubs.acs.org.

■ AUTHOR INFORMATION

Corresponding Author

*E-mail: kpete@bnl.gov.

Present Address

♦Department of Energy and Materials Engineering, Dongguk University-Seoul, Seoul 100-715, Republic of Korea.

Notes

The authors declare no competing financial interest.

■ ACKNOWLEDGMENTS

Research supported as part of the Northeastern Center for Chemical Energy Storage (NECCES), an Energy Frontier Research Center funded by the U.S. Department of Energy, Office of Basic Energy Sciences under Award DE-SC0001294, including matching support from NYSTAR-NYSDED. This research utilized the facilities at the Center for Functional Nanomaterials, Brookhaven National Laboratory, which is supported by the U.S. Department of Energy, Office of Basic Energy Sciences, under Contract No. DE-AC02-98CH10886. Use of the National Synchrotron Light Source, Brookhaven National Laboratory, was supported by the U.S. Department of Energy, Office of Science, Office of Basic Energy Sciences, under Contract No. DE-AC02-98CH10886. Research conducted at ORNL's Spallation Neutron Source was sponsored by the Scientific User Facilities Division, Office of Basic Energy Sciences, US Department of Energy. M. Dawber and J. Sinsheimer are thanked for use of their instrumentation and guidance in the collection of impedance spectroscopy data. P.K. would like to acknowledge the support and guidance provided by the EFRC directors and Intercalation Thrust Leaders, C. P. Grey and M. S. Whittingham, as well as discussions on oxynitrides with G. Ceder. The authors thank the NSLS beamline scientists at X7B and X19A for their technical support.

■ REFERENCES

(1) Pan, H. L.; Hu, Y. S.; Chen, L. Q. *Energy Environ. Sci.* **2013**, *6*, 2338.
(2) Palomares, V.; Serras, P.; Villaluenga, I.; Hueso, K. B.; Carretero-Gonzalez, J.; Rojo, T. *Energy Environ. Sci.* **2012**, *5*, 5884.
(3) Kim, S. W.; Seo, D. H.; Ma, X. H.; Ceder, G.; Kang, K. *Adv. Energy Mater.* **2012**, *2*, 710.
(4) Braconnier, J. J.; Delmas, C.; Fouassier, C.; Hagenmuller, P. *Mater. Res. Bull.* **1980**, *15*, 1797.
(5) Delmas, C.; Fouassier, C.; Hagenmuller, P. *Physica B+C (Amsterdam)* **1980**, *99*, 81.
(6) Braconnier, J. J.; Delmas, C.; Hagenmuller, P. *Mater. Res. Bull.* **1982**, *17*, 993.
(7) Didier, C.; Guignard, M.; Denage, C.; Szajwaj, O.; Ito, S.; Saadoune, I.; Darriet, J.; Delmas, C. *Electrochem. Solid-State Lett.* **2011**, *14*, A75.
(8) Komaba, S.; Takei, C.; Nakayama, T.; Ogata, A.; Yabuuchi, N. *Electrochem. Commun.* **2010**, *12*, 355.

(9) Zhou, Y. N.; Ding, J. J.; Nam, K. W.; Yu, X. Q.; Bak, S. M.; Hu, E. Y.; Liu, J.; Bai, J. M.; Li, H.; Fu, Z. W.; Yang, X. Q. *J. Mater. Chem. A* **2013**, *1*, 11130.
(10) Caballero, A.; Hernan, L.; Morales, J.; Sanchez, L.; Pena, J. S.; Aranda, M. A. G. *J. Mater. Chem.* **2002**, *12*, 1142.
(11) Berthelot, R.; Carlier, D.; Delmas, C. *Nat. Mater.* **2011**, *10*, 74.
(12) Yabuuchi, N.; Kajiyama, M.; Iwatate, J.; Nishikawa, H.; Hitomi, S.; Okuyama, R.; Usui, R.; Yamada, Y.; Komaba, S. *Nat. Mater.* **2012**, *11*, 512.
(13) Moreau, P.; Guyomard, D.; Gaubicher, J.; Boucher, F. *Chem. Mater.* **2010**, *22*, 4126.
(14) Lee, K. T.; Ramesh, T. N.; Nan, F.; Botton, G.; Nazar, L. F. *Chem. Mater.* **2011**, *23*, 3593.
(15) Goodenough, J. B.; Hong, H. Y. P.; Kafalas, J. A. *Mater. Res. Bull.* **1976**, *11*, 203.
(16) Delmas, C.; Cherkaoui, F.; Nadiri, A.; Hagenmuller, P. *Mater. Res. Bull.* **1987**, *22*, 631.
(17) Plashnitsa, L. S.; Kobayashi, E.; Noguchi, Y.; Okada, S.; Yamaki, J. *J. Electrochem. Soc.* **2010**, *157*, A536.
(18) Jian, Z. L.; Zhao, L.; Pan, H. L.; Hu, Y. S.; Li, H.; Chen, W.; Chen, L. Q. *Electrochem. Commun.* **2012**, *14*, 86.
(19) Barker, J.; Saidi, M. Y.; Swoyer, J. L. *Electrochem. Solid-State Lett.* **2003**, *6*, A1.
(20) Gover, R.; Bryan, A.; Burns, P.; Barker, J. *Solid State Ionics* **2006**, *177*, 1495.
(21) Chihara, K.; Kitajou, A.; Gocheva, I. D.; Okada, S.; Yamaki, J. *J. Power Sources* **2013**, *227*, 80.
(22) Ellis, B. L.; Makahnouk, W. R. M.; Makimura, Y.; Toghill, K.; Nazar, L. F. *Nat. Mater.* **2007**, *6*, 749.
(23) Recham, N.; Chotard, J. N.; Dupont, L.; Djellab, K.; Armand, M.; Tarascon, J. M. *J. Electrochem. Soc.* **2009**, *156*, A993.
(24) Chen, H. L.; Hao, Q.; Zivkovic, O.; Hautier, G.; Du, L. S.; Tang, Y. Z.; Hu, Y. Y.; Ma, X. H.; Grey, C. P.; Ceder, G. *Chem. Mater.* **2013**, *25*, 2777.
(25) Barpanda, P.; Oyama, G.; Ling, C. D.; Yamada, A. *Chem. Mater.* **2014**, *26*, 1297.
(26) Liu, J.; Yu, X. Q.; Hu, E. Y.; Nam, K. W.; Yang, X. Q.; Khalifah, P. G. *Chem. Mater.* **2013**, *25*, 3929.
(27) Conanec, R.; Feldmann, W.; Marchand, R.; Laurent, Y. *J. Solid State Chem.* **1996**, *121*, 418.
(28) Feldmann, W. *Z. Chem. (Stuttgart, Ger.)* **1987**, *27*, 182.
(29) Feldmann, W. *Z. Chem. (Stuttgart, Ger.)* **1987**, *27*, 100.
(30) Zatovsky, I. V.; Vorobjova, T. V.; Domasevitch, K. V.; Ogorodnyk, I. V.; Slobodyanik, N. S. *Acta Crystallogr., Sect. E: Struct. Rep. Online* **2006**, *62*, 32.
(31) Barker, J. U.S. Patent 2008/0187831 A1.
(32) Lee, M. S.; Kang, J. K.; Kim, S. J. *Bull. Korean Chem. Soc.* **2012**, *33*, 2083.
(33) Yao, Y. F. Y.; Kummer, J. T. *J. Inorg. Nucl. Chem.* **1967**, *29*, 2453.
(34) Hammersley, A. P.; Svensson, S. O.; Hanfland, M.; Fitch, A. N.; Hausermann, D. *High Pressure Res.* **1996**, *14*, 235.
(35) Hu, E.; Bak, S.-M.; Liu, J.; Yu, X.; Zhou, Y.; Ehrlich, S. N.; Yang, X.-Q.; Nam, K.-W. *Chem. Mater.* **2014**, *26*, 1108.
(36) Neuefeind, J.; Feygenson, M.; Carruth, J.; Hoffmann, R.; Chipley, K. K. *Nucl. Instrum. Methods Phys. Res., Sect. B* **2012**, *287*, 68.
(37) Ravel, B.; Newville, M. *J. Synchrotron Radiat* **2005**, *12*, 537.
(38) Rodriguez-Carvajal, J.; Gonzalez-Platas, J. *Acta Crystallogr., Sect. A* **2002**, *A58*, C87.
(39) Adams, S. *Acta Crystallogr., Sect. B* **2001**, *57*, 278.
(40) Momma, K.; Izumi, F. *J. Appl. Crystallogr.* **2008**, *41*, 653.
(41) Thangadurai, V.; Adams, S.; Weppner, W. *Chem. Mater.* **2004**, *16*, 2998.
(42) Adams, S. *J. Solid State Electrochem.* **2010**, *14*, 1787.
(43) Adams, S.; Rao, R. P. *Phys. Status Solidi A* **2011**, *208*, 1746.
(44) Janssen, Y.; Middlemiss, D. S.; Bo, S. H.; Grey, C. P.; Khalifah, P. G. *J. Am. Chem. Soc.* **2012**, *134*, 12516.
(45) Kresse, G.; Furthmuller, J. *Phys. Rev. B* **1996**, *54*, 11169.
(46) Blochl, P. E. *Phys. Rev. B* **1994**, *50*, 17953.
(47) Dudarev, S. L.; Botton, G. A.; Savrasov, S. Y.; Humphreys, C. J.; Sutton, A. P. *Phys. Rev. B* **1998**, *57*, 1505.
(48) Sanchez, J. M.; Ducastelle, F.; Gratias, D. *Physica A* **1984**, *128*, 334.
(49) Van der Ven, A.; Thomas, J. C.; Xu, Q. C.; Swoboda, B.; Morgan, D. *Phys. Rev. B* **2008**, 78.
(50) Wood, R. M.; Palenik, G. J. *Inorg. Chem.* **1999**, *38*, 3926.
(51) Ohzuku, T.; Ueda, A.; Yamamoto, N. *J. Electrochem. Soc.* **1995**, *142*, 1431.
(52) Neudecker, B. J.; Weppner, W. *J. Electrochem. Soc.* **1996**, *143*, 2198.
(53) Aono, H.; Sugimoto, E. *J. Am. Ceram. Soc.* **1996**, *79*, 2786.
(54) Brown, I. D. *Chem. Rev. (Washington, DC, U. S.)* **2009**, *109*, 6858.
(55) Van der Ven, A.; Bhattacharya, J.; Belak, A. A. *Acc. Chem. Res.* **2013**, *46*, 1216.
(56) Liu, J. et al. Unpublished results.
(57) Ong, S. P.; Jain, A.; Hautier, G.; Kang, B.; Ceder, G. *Electrochem. Commun.* **2010**, *12*, 427.
(58) Reinert, A. A.; Payne, C.; Wang, L. M.; Ciston, J.; Zhu, Y. M.; Khalifah, P. G. *Inorg. Chem.* **2013**, *52*, 8389.
(59) Hewett, C. L.; Cheng, Y. B.; Muddle, B. C.; Trigg, M. B. *J. Eur. Ceram. Soc.* **1998**, *18*, 417.
(60) Delacourt, C.; Poizot, P.; Tarascon, J.-M.; Masquelier, C. *Nat. Mater.* **2005**, *4*, 254.

Supporting Information

Ionic conduction in cubic $Na_3TiP_3O_9N$, a secondary Na-ion battery cathode with extremely low volume change

Jue Liu[§], Donghee Chang[||], Pamela Whitfield[&], Yuri Janssen[§], Xiqian Yu[†], Yongning Zhou[†], Jianming Bai[#], Jonathan Ko[‡], Kyung-Wan Nam[†], Lijun Wu[⊥], Yimei Zhu[⊥], Mikhail Feygenson[&], Glenn Amatucci[‡], Anton Van der Ven[+,||], Xiao-Qing Yang[†], Peter Khalifah [*, §, †]

[§] Department of Chemistry, State University of New York at Stony Brook, Stony Brook, United States

[||]Department of Materials Science and Engineering, University of Michigan, Ann Arbor, MI, United States

[&]Chemical and Engineering Materials Division, Oak Ridge National Laboratory, Oak Ridge, TN, 37830, United States

[†] Department of Chemistry, Brookhaven National Laboratory, Uptown, NY, United States

[#] Photon Science Division, Brookhaven National Laboratory, Uptown, NY, United States

[‡] Energy Storage Research Group, Department of Materials Science and Engineering, Rutgers, The State University of New Jersey, 671 US Hwy 1, North Brunswick, NJ , United States

[+] Materials Department, University of California Santa Barbara, Santa Barbara, CA, 93106, United States

[⊥] Condensed Matter Physics and Material Science Department, Brookhaven National Laboratory, Upton, NY, United States

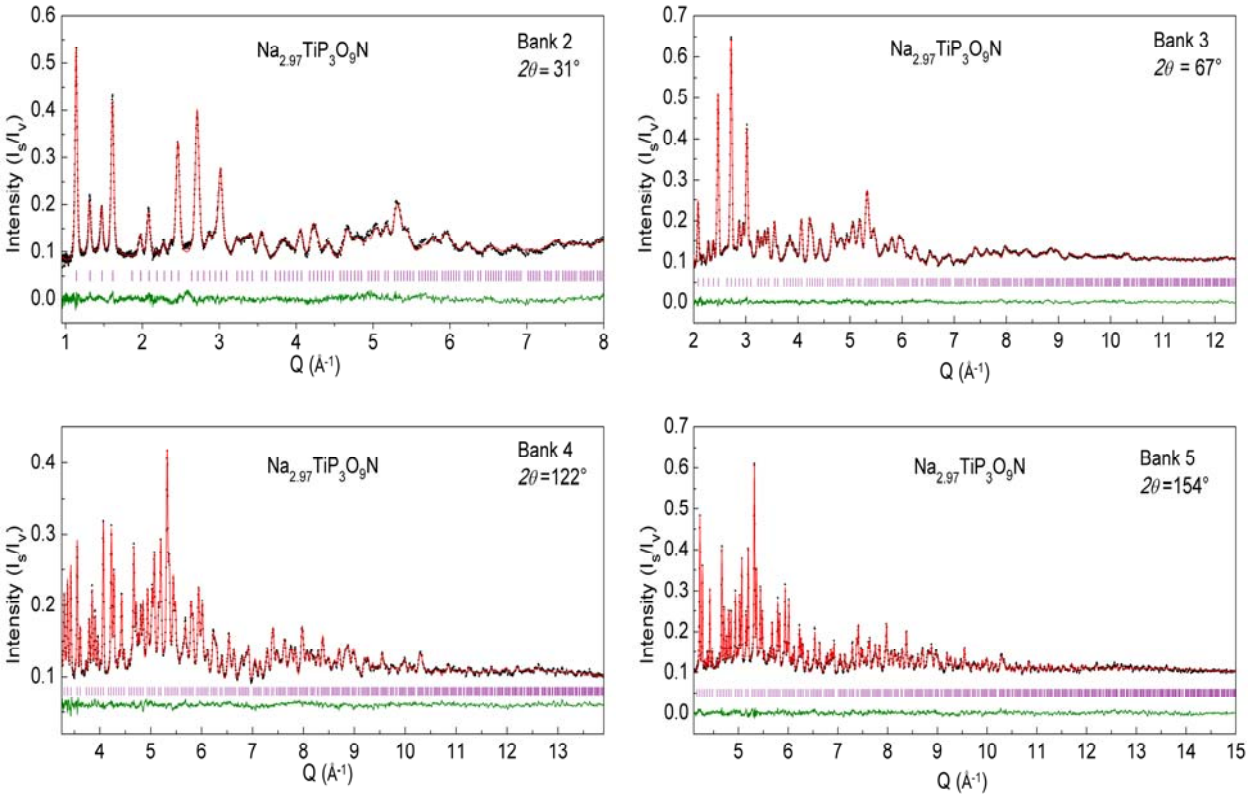

Figure S1. Rietveld refinement of TOF neutron diffraction data for $Na_3TiP_3O_9N$.

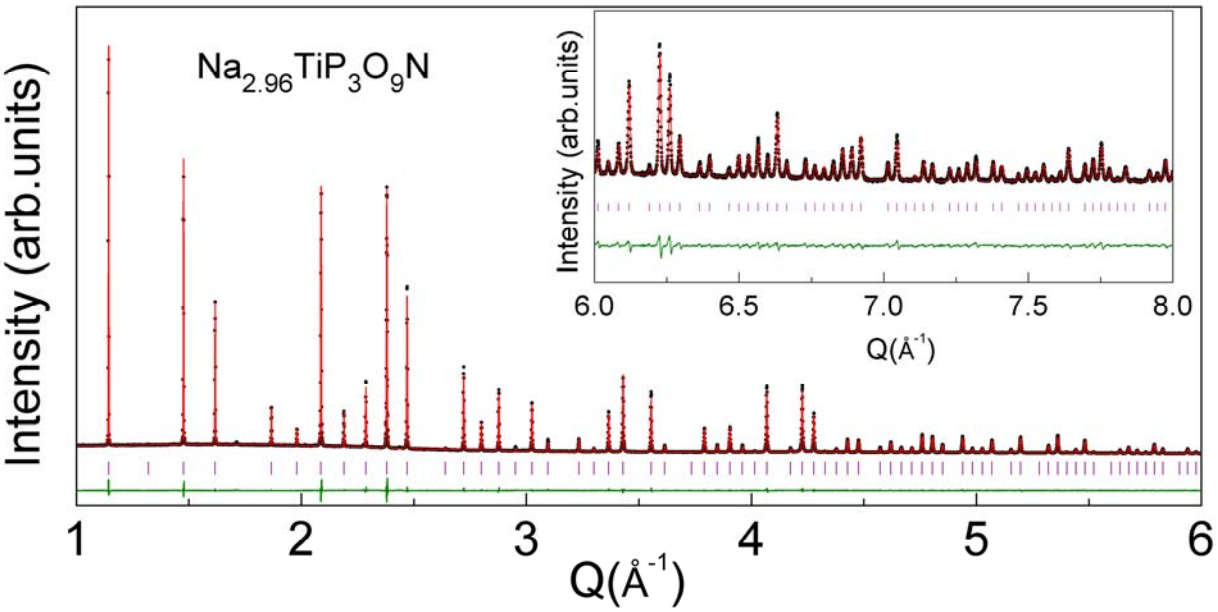

Figure S2. Rietveld refinement of synchrotron XRD data (λ = 0.77878 Å) for $Na_3TiP_3O_9N$.

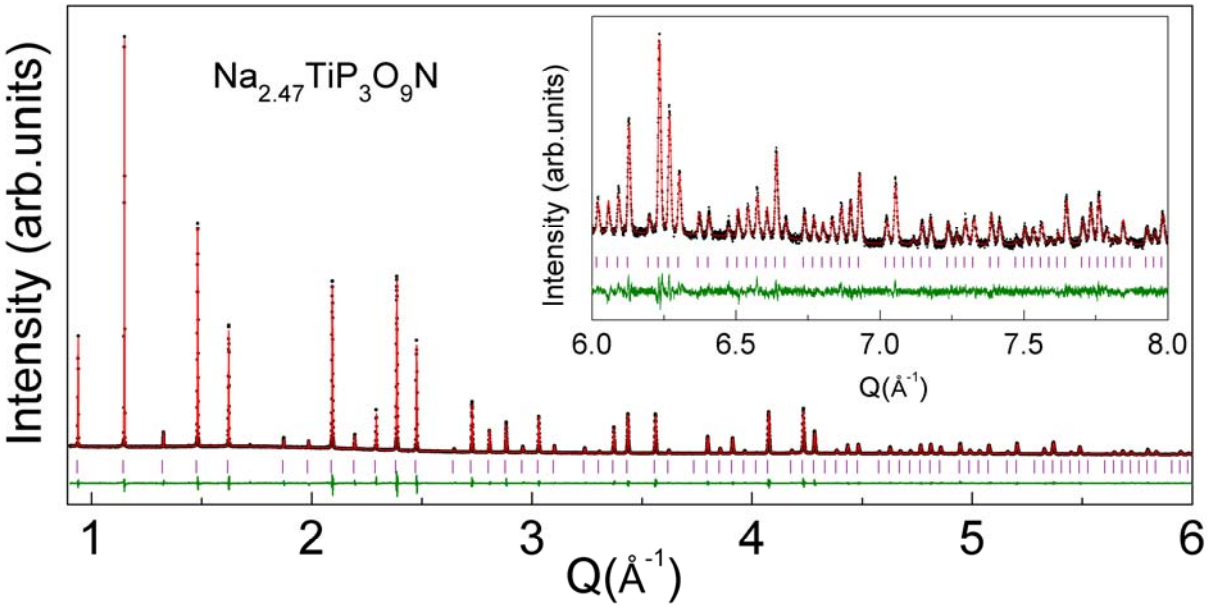

Figure S3. Rietveld refinement of synchrotron XRD data (λ = 0.77767Å) for $Na_{2.5}TiP_3O_9N$.

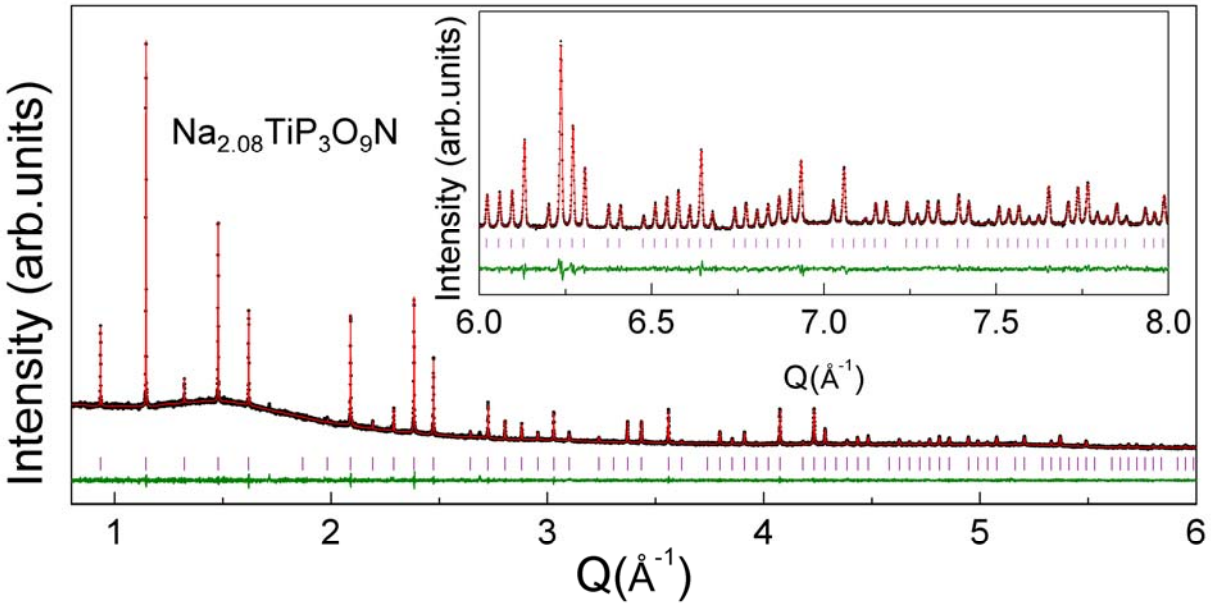

Figure S4. Rietveld refinement of synchrotron XRD data (λ = 0.77875 Å) for $Na_2TiP_3O_9N$.

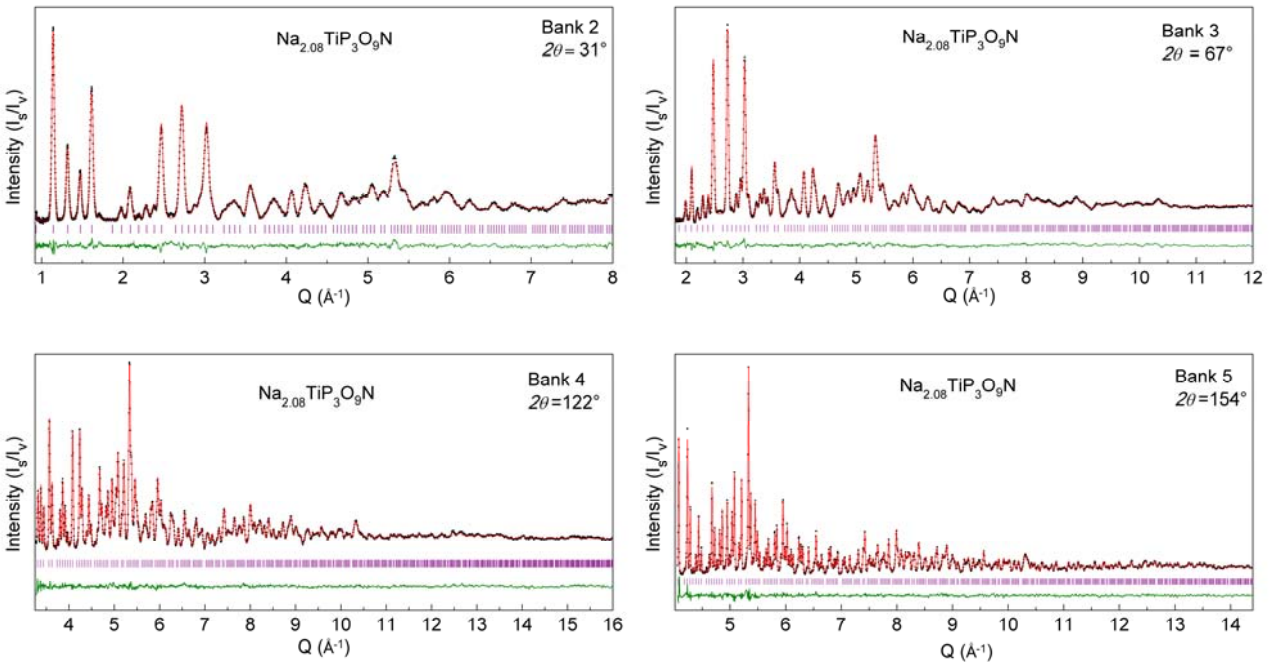

Figure S5. Rietveld refinement of TOF neutron diffraction data for $Na_2TiP_3O_9N$.

Table S1. Summary of Rietveld refinement results

Radiation	XRD	XRD	XRD	TOF neutron	TOF neutron
λ	0.77878 Å	0.77767Å	0.77875 Å	0.1-3 Å	0.1-3 Å
Formula	$Na_{2.96}TiP_3O_9N$	$Na_{2.47}TiP_3O_9N$	$Na_{2.08}TiP_3O_9N$	$Na_{2.97}TiP_3O_9N$	$Na_{2.08}TiP_3O_9N$
Crystal system	Cubic	Cubic	Cubic	Cubic	Cubic
Space group	*$P2_13$(198)*	*$P2_13$(198)*	*$P2_13$(198)*	*$P2_13$(198)*	*$P2_13$(198)*
Lattice a	9.5192 (3) Å	9.5161 (4) Å	9.5046 (2) Å	9.5180 (2) Å	9.5092 (2) Å
Cell volume	862.58 (7) $Å^3$	861.74 (11) $Å^3$	858.60 (6) $Å^3$	862.26 (5) $Å^3$	859.86 (5) $Å^3$
R_{wp}	2.81%	3.68%	4.45%	2.34%	2.64%
R_p	1.88%	2.56%	2.60%	2.15%	1.59%
χ^2	3.50	3.99	3.75	1.21	1.66

Table S2. Rietveld refinement results for $Na_3TiP_3O_9N$ using TOF neutron diffraction data measured at 300 K in Ar (NOMAD, SNS).

Atom	Wyck.	*x*	*y*	*z*	Occ.	B_{eq} ($Å^2$)
Na1	4a	0.01129(34)	0.01129(34)	0.01129(34)	0.966(37)	2.49
Na2	4a	0.39430(27)	0.39430(27)	0.39430(27)	1	1.49
Na3	4a	0.80249(36)	0.80249(36)	0.80249(36)	1	2.99
Ti1	4a	0.58186(25)	0.58186(25)	0.58186(25)	1	0.95
P1	12b	0.08461(16)	0.24474(15)	0.33282(18)	1	0.74
O1	12b	0.02187(14)	0.84785(14)	0.23148(13)	1	1.12
O2	12b	0.00640(15)	0.11152(14)	0.37448(14)	1	1.26
O3	12b	0.16837(15)	0.30919(18)	0.45015(14)	1	1.43
N1	4a	0.19905(9)	0.19905(9)	0.19905(9)	1	0.79

Atom	U_{11}($Å^2$)	U_{22}($Å^2$)	U_{33}($Å^2$)	U_{12}($Å^2$)	U_{13}($Å^2$)	U_{23}($Å^2$)
Na1	0.0348(24)	0.0348(24)	0.0348(24)	0.0210(29)	0.0210(29)	0.0210(29)
Na2	0.0209(16)	0.0209(16)	0.0209(16)	0	0	0
Na3	0.0459(25)	0.0459(25)	0.0459(25)	0.0247(35)	0.0247(35)	0.0247(35)
Ti1	0.0131(12)	0.0131(12)	0.0131(12)	0.0045(13)	0.0045(13)	0.0045(13)
P1	0.0136(12)	0.0064(11)	0.0095(12)	0.0024(8)	0.0007(7)	-0.0007(7)
O1	0.0158(12)	0.0140(13)	0.0153(12)	-0.0102(8)	0.0012(8)	-0.0034(8)
O2	0.0153(12)	0.0120(12)	0.0157(13)	-0.0015(7)	0.0014(8)	0.0028(7)
O3	0.0207(14)	0.0280(15)	0.0110(11)	-0.0050(9)	-0.0011(8)	-0.0045(9)
N1	0.0107(8)	0.0107(8)	0.0107(8)	-0.0008(4)	-0.0008(4)	-0.0008(4)

Table S3. Rietveld refinement results for $Na_3TiP_3O_9N$ using synchrotron X-ray diffraction data measured at 300 K in air. (X14A, NSLS).

Atom	Wyck.	*x*	*y*	*z*	Occ.	B_{eq} (Å^2)
Na1	4a	0.01231(18)	0.01231(18)	0.01231(18)	0.963(10)	1.61(13)
Na2	4a	0.39364(21)	0.39364(21)	0.39364(21)	1	1.53(11)
Na3	4a	0.80348(25)	0.80348(25)	0.80348(25)	1	1.93(10)
Ti1	4a	0.58129(8)	0.58129(8)	0.58129(8)	1	0.59(8)
P1	12b	0.08636(12)	0.24551(13)	0.33344(13)	1	0.52(8)
O1	12b	0.02168(26)	0.84884(27)	0.23382(40)	1	1.01(10)
O2	12b	0.00552(30)	0.11398(27)	0.37635(27)	1	0.77(10)
O3	12b	0.16837(27)	0.30995(26)	0.44508(43)	1	0.90(10)
N1	4a	0.19893(32)	0.19893(32)	0.19893(32)	1	0.57(20)

Table S4. Rietveld refinement results for $Na_{2.5}TiP_3O_9N$ using synchrotron X-ray diffraction data measured at 300 K in air. (X14A, NSLS).

Atom	Wyck.	*x*	*y*	*z*	Occ.	B_{eq} (Å^2)
Na1	4a	0.01408(55)	0.01408(55)	0.01408(55)	0.474(10)	2.96(29)
Na2	4a	0.39080(23)	0.39080(23)	0.39080(23)	1	2.33(16)
Na3	4a	0.80829(24)	0.80829(24)	0.80829(24)	1	1.97(13)
Ti1	4a	0.58318(10)	0.58318(10)	0.58318(10)	1	0.68(11)
P1	12b	0.08461(14)	0.24248(15)	0.33057(14)	1	0.58(11)
O1	12b	0.02430(30)	0.83715(32)	0.24097(39)	1	0.75(13)
O2	12b	0.00869(31)	0.10782(44)	0.37752(38)	1	0.77(10)
O3	12b	0.16696(32)	0.30557(33)	0.44779(34)	1	0.97(13)
N1	4a	0.19730(36)	0.19730(36)	0.19730(36)	1	1.25(19)

Table S5. Rietveld refinement results for $Na_2TiP_3O_9N$ using TOF neutron diffraction data measured at 300 K in Ar (NOMAD, SNS).

Atom	Wyck.	*x*	*y*	*z*	Occ.	B_{eq} (Å^2)
Na1	4a	0.0064(27)	0.0064(27)	0.0064(27)	0.085(4)	2.17(98)
Na2	4a	0.39123(20)	0.39123(20)	0.39123(20)	1	1.10
Na3	4a	0.81376(23)	0.81376(23)	0.81376(23)	1	2.33
Ti1	4a	0.58474(21)	0.58474(21)	0.58474(21)	1	1.10
P1	12b	0.08461(14)	0.23983(12)	0.32989(14)	1	0.62
O1	12b	0.02576(11)	0.83577(12)	0.23872(10)	1	0.94
O2	12b	0.00893(12)	0.10335(11)	0.37382(11)	1	0.89
O3	12b	0.16634(12)	0.30500(13)	0.44710(11)	1	1.40
N1	4a	0.19616(7)	0.19616(7)	0.19616(7)	1	0.72

Atom	U_{11}(Å^2)	U_{22}(Å^2)	U_{33}(Å^2)	U_{12}(Å^2)	U_{13}(Å^2)	U_{23}(Å^2)
Na1	-	-	-	-	-	-
Na2	0.0139(11)	0.0139(11)	0.0139(11)	0	0	0
Na3	0.0296(13)	0.0296(13)	0.0296(13)	0.0053(19)	0.0053(19)	0.0053(19)
Ti1	0.0140(10)	0.0140(10)	0.0140(10)	0.0013(11)	0.0013(11)	0.0013(11)
P1	0.0104(9)	0.0063(8)	0.0069(8)	-0.0008(4)	-0.0002(5)	-0.0021(6)
O1	0.0127(8)	0.0134(1)	0.0095(8)	-0.0061(5)	-0.0002(6)	-0.0022(7)
O2	0.0112(8)	0.01096(9)	0.0118(8)	-0.0053(4)	0.0016(7)	0.0005(6)
O3	0.0194(11)	0.0229(10)	0.0109(8)	-0.0067(6)	-0.0039(7)	-0.0035(7)
N1	0.0090(4)	0.0090(4)	0.0090(4)	0.0011(4)	0.0011(4)	0.0011(4)

Table S6 Rietveld refinement results for $Na_2TiP_3O_9N$ using synchrotron X-ray diffraction data measured at 300 K in air (X14A, NSLS).

Atom	Wyck.	*x*	*y*	*z*	Occ.	B_{eq} (Å^2)
Na1	4a	0.01232(18)	0.0026(35)	0.0026(35)	0.085*	2.17*
Na2	4a	0.39090(25)	0.39090(25)	0.39090(25)	1	1.51(15)
Na3	4a	0.81422(32)	0.81422(32)	0.81422(32)	1	1.80(15)
Ti1	4a	0.58518(10)	0.58518(10)	0.58518(10)	1	0.49(13)
P1	12b	0.08541(15)	0.23998(11)	0.33038(15)	1	0.43(14)
O1	12b	0.02451(40)	0.83665(45)	0.23960(42)	1	0.67(15)
O2	12b	0.00848(40)	0.10458(41)	0.37511(42)	1	0.68(14)
O3	12b	0.16587(47)	0.30312(46)	0.44508(43)	1	1.21(16)
N1	4a	0.19524(51)	0.19524(51)	0.19524(51)	1	0.57(20)

* fixed to refinement result of neutron diffraction data

Table S7. Selected bond distances (Å) for $Na_3TiP_3O_9N$, $Na_{2.5}TiP_3O_9N$ and $Na_2TiP_3O_9N$.

	$Na_{2.96}TiP_3O_9N$ (XRD)	**$Na_{2.97}TiP_3O_9N$** (TOF neutron)	**$Na_{2.5}TiP_3O_9N$** (XRD)	**$Na_{2.08}TiP_3O_9N$** (XRD)	**$Na_{2.08}TiP_3O_9N$** (TOF neutron)
Na1 – O1 (×3)	2.6220(34)	2.6120(14)	2.7397(35)	2.7661(83)	2.7480(61)
Na1 – O3 (×3)	2.6091(33)	2.5998(44)	2.6527(74)	2.577(41)	2.559(32)
Na1 – N	3.0767(60)	3.0953(58)	3.020(11)	3.112(58)	3.130(45)
Na2 – O2 (×3)	2.4358(36)	2.4465(36)	2.4737(46)	2.4832(44)	2.4991(28)
Na2 – O3 (×3)	2.3464(33)	2.3586(31)	2.3429(38)	2.3545(43)	2.3512(23)
Na3 – O1 (×3)	3.0697(43)	3.0473(52)	3.0723(45)	3.1071(48)	3.1257(34)
Na3 – O3 (×3)	2.3765(38)	2.3715(40)	2.3332(40)	2.3096(43)	2.2834(24)
Ti – O1 (×3)	1.9642(36)	1.9824(25)	1.9207(36)	1.8985(36)	1.9245(21)
Ti – O2 (×3)	2.0344(27)	2.0190(30)	1.9865(41)	1.9688(34)	1.9684(25)
P – O1	1.5614(31)	1.5378(21)	1.5327(35)	1.5449(37)	1.5361(17)
P – O2	1.5256(29)	1.5229(20)	1.5374(41)	1.5355(35)	1.5416(16)
P – O3	1.4792(30)	1.5030(21)	1.4896(35)	1.4723(40)	1.4935(17)
P – N	1.7274(15)	1.7311(17)	1.7155(17)	1.7133(18)	1.7073(13)

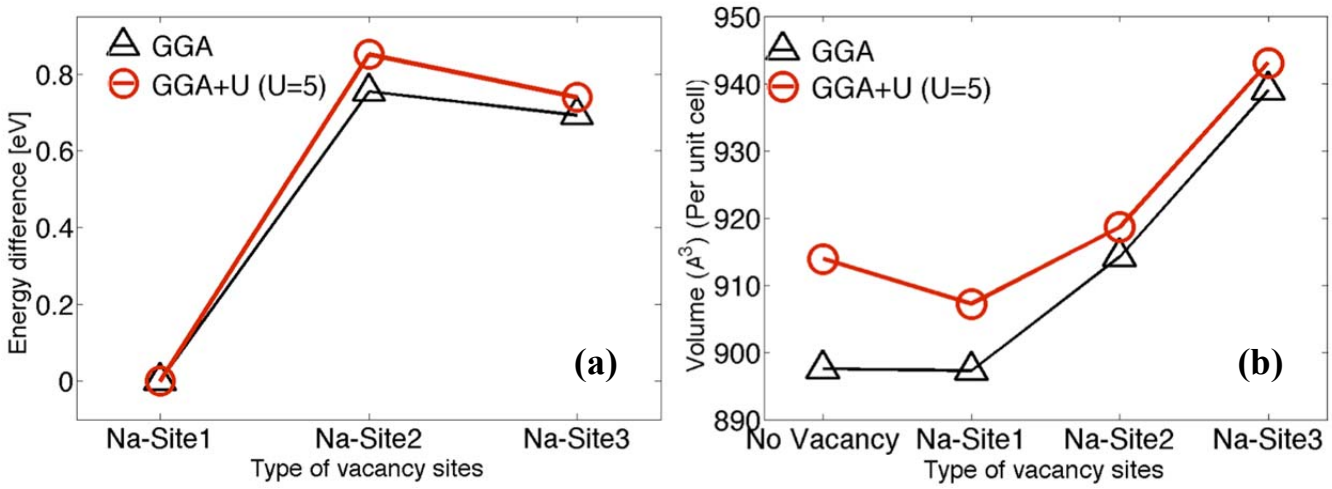

Figure S6. Calculated free energy (a) and volume change (b) associated with Na removal from each of the three crystallographic sites of $Na_3TiP_3O_9N$ (energies and volumes are per primitive unit cell containing four $Na_3TiP_3O_9N$ formula units).

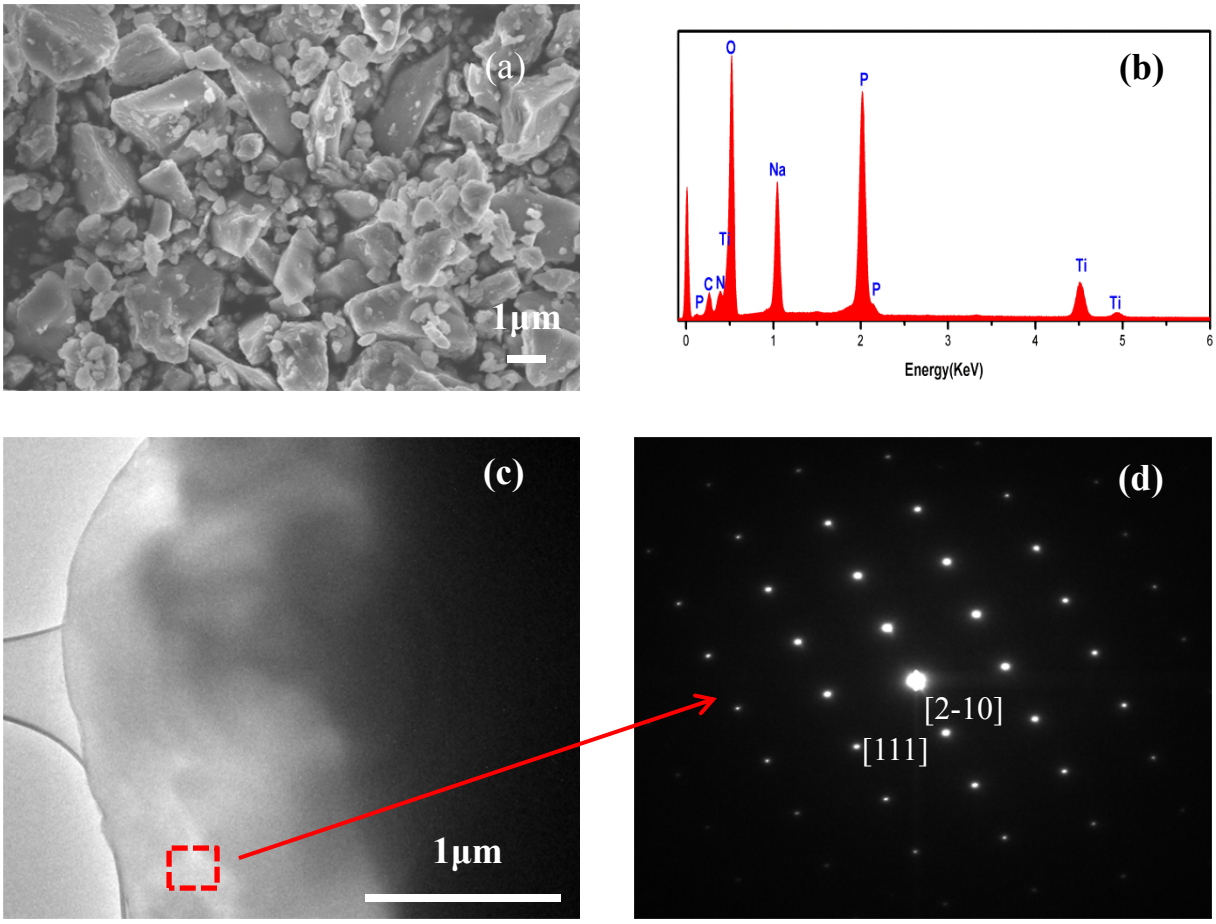

Figure S7. (a) SEM image, (b) EDX pattern, (c) TEM image, and (d) electron diffraction pattern from as-prepared $Na_3TiP_3O_9N$ powder.

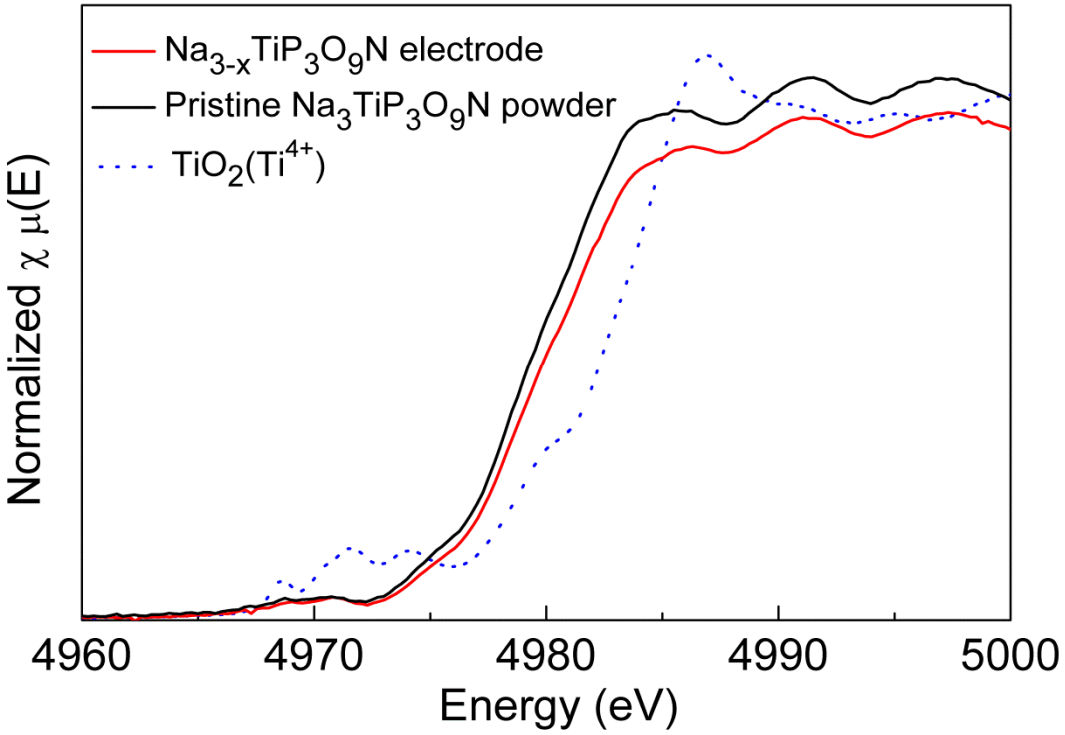

Figure S8. Ti *K*-edge XANES spectra of pristine $Na_3TiP_3O_9N$ and partially oxidized $Na_{3-x}TiP_3O_9N$ after ball milling for 1 hour.

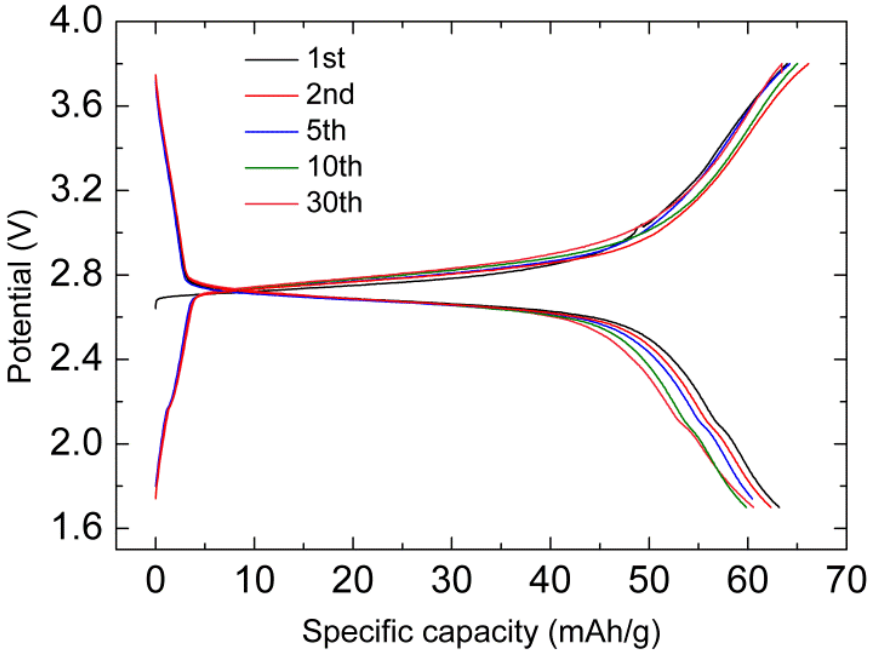

Figure S9. Charge-discharge profile of $Na_3TiP_3O_9N$ (ball milled for 1 hour) cycled against Na at C/20.

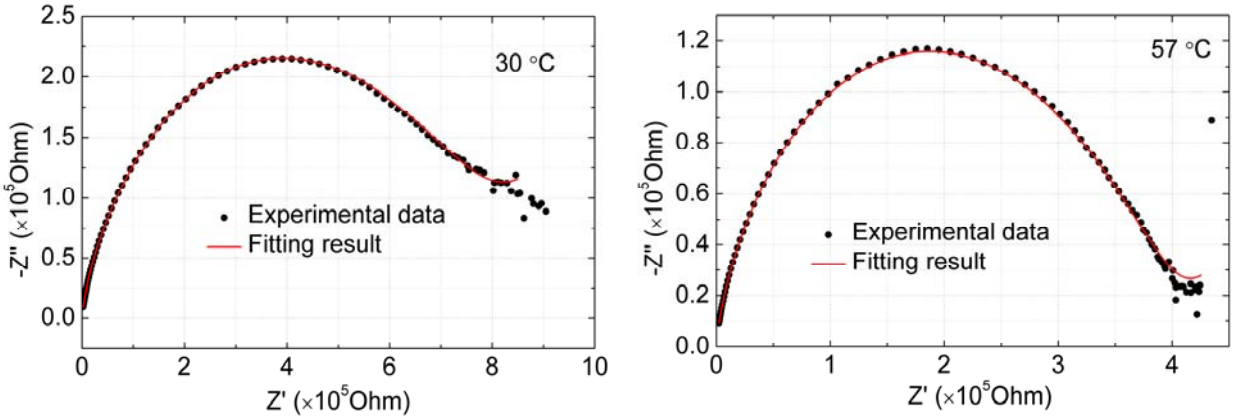

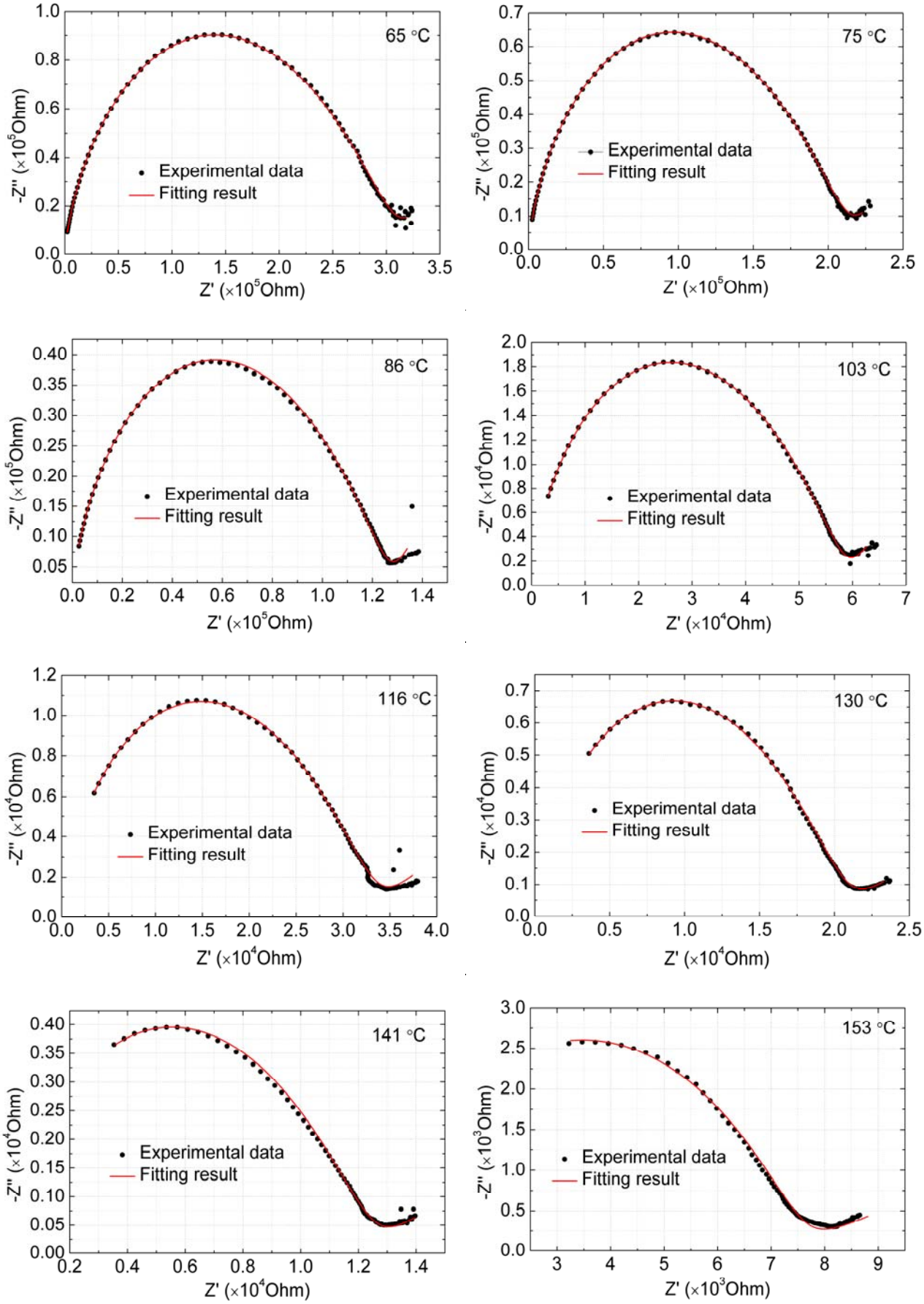
65 °C
75 °C
86 °C
103 °C
116 °C
130 °C
141 °C
153 °C
Experimental data
Fitting result
-Z'' (×10^5Ohm)
Z' (×10^5Ohm)
-Z'' (×10^4Ohm)
Z' (×10^4Ohm)
-Z'' (×10^3Ohm)
Z' (×10^3Ohm)

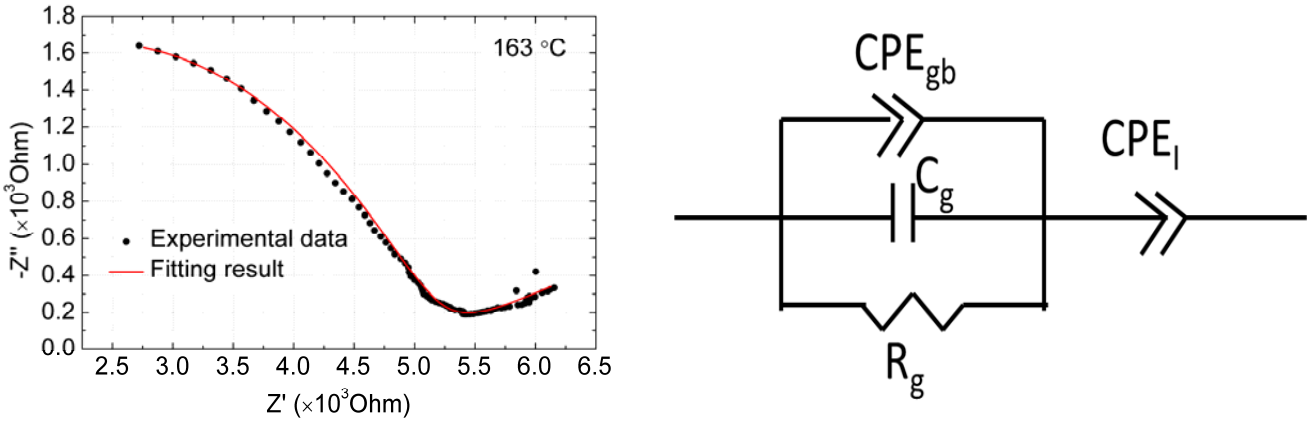

Figure S10. Fits of AC impedance spectra collected at temperatures from 30 – 163 °C using frequencies of 20 Hz – 2 MHz, and the equivalent circuit used for modeling the data. Refined parameters are reported in Table S8.

The parameters in this equivalent circuit are closely associated with physical response mechanisms permitted within pellet the measurement geometry. R_g represents the bulk resistance of the $Na_3TiP_3O_9N$ electrolyte, C_g represents the capacitance between the two metal electrodes, CPE_{gb} is a constant-phase-angle element that represents sodium ions moving into (or across) grain boundaries, and CPE_I is a constant-phase-angle element used to model the diffusion of sodium ions into the contacts. The first three elements allow the high-frequency arc to be described, while the CPE_I is required to model the low frequency tail of the spectrum.

Table S8. Fitting results of T-dependent ac impedance data.

T (°C)	R_g (Ω)	Δ R_g (%)	C_g (F)	CPE_{gb} B1 (Ω S^{-n1})	CPE_{gb} n1	CPE_I B2 (Ω S^{-n2})	CPE_I n2
30	794790	0.226	6.97E-12	4.33E-09	0.5449	6.37E-07	0.45228
57	402160	0.485	6.23E-12	3.20E-09	0.5682	3.40E-06	0.40031
65	306230	0.106	6.28E-12	3.30E-09	0.5635	7.22E-06	0.36441
75	211990	0.119	6.28E-12	3.46E-09	0.5628	8.72E-06	0.36990
86	127070	0.377	6.06E-12	3.77E-09	0.5670	7.39E-06	0.47269
103	58355	0.266	6.30E-12	5.60E-09	0.5547	2.62E-05	0.36451
116	32646	0.510	7.00E-12	7.88E-09	0.5424	5.07E-05	0.24503
130	20074	0.257	7.41E-12	1.11E-08	0.5311	0.000101	0.19595
141	12105	0.748	6.81E-12	1.38E-08	0.5336	0.000172	0.19916
153	7319	0.108	7.42E-12	9.99E-09	0.5558	0.000269	0.17713
163	4929	1.184	5.48E-12	8.93E-09	0.5860	0.00034	0.17380

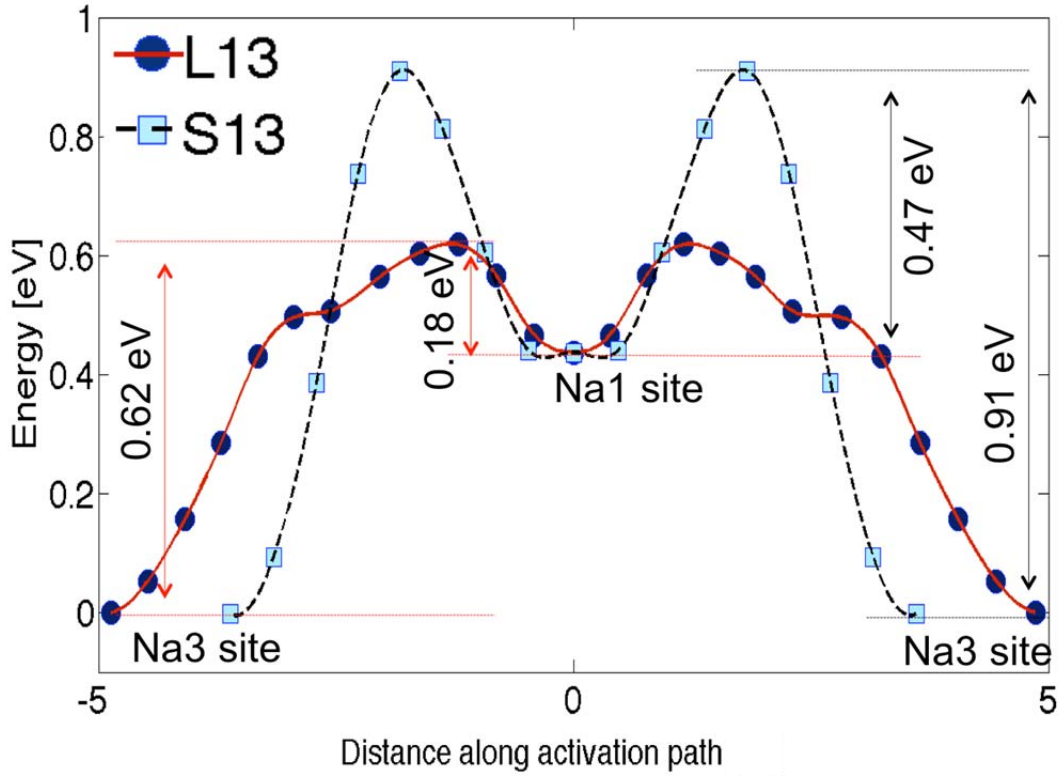

Figure S11. Energies for points along the short (S13) and long (L13) Na1-Na3 pathways calculated by simple GGA methods without the inclusion of a Hubbard U term. Distances are given in Å.

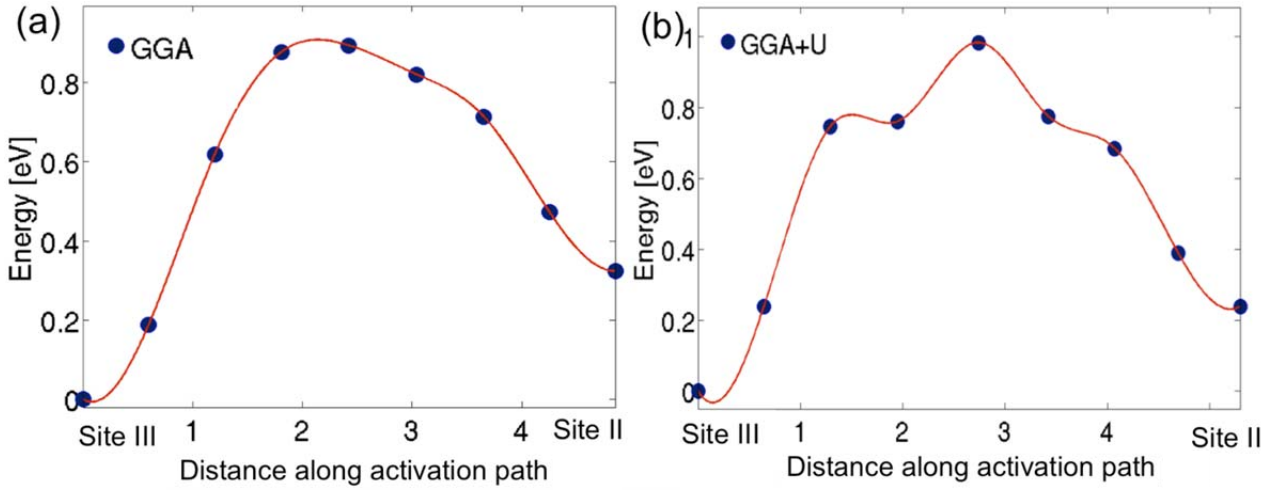

Figure S12. Energies for points along the Na1-Na2 type pathway (P12). Distances are given in Å. (a) Energies are calculated by GGA (b) Energies calculated by GGA+U (U=5 eV).

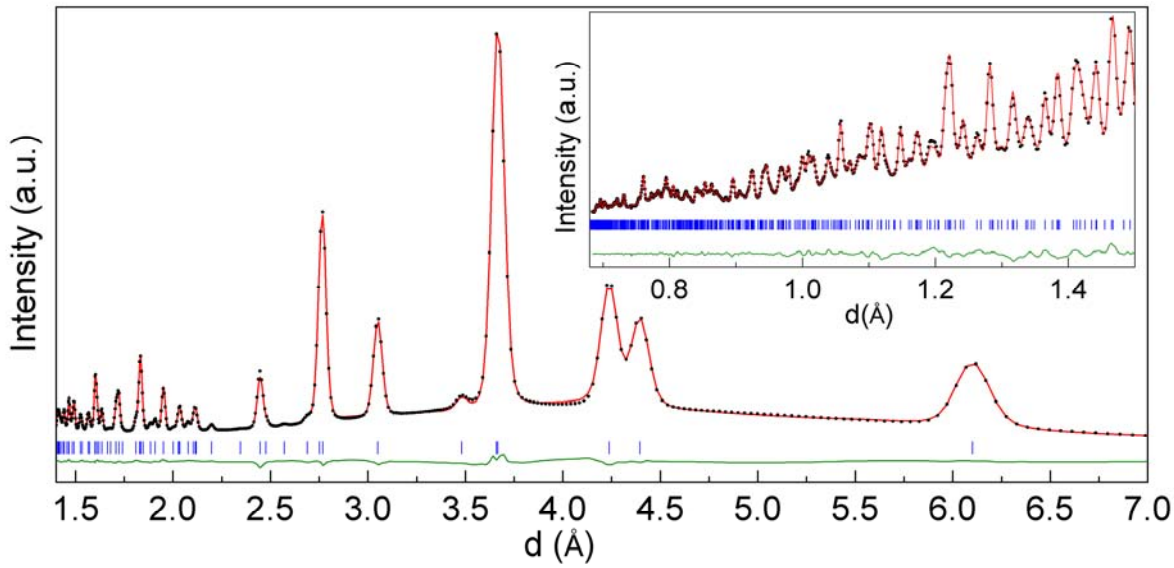

Figure S13. Rietveld refinement of final diffraction pattern (scan number 168, λ = 0.3196 Å) containing $NaTi_2(PO_4)_3$ at the conclusion of the *in situ* heating experiment for $Na_3TiP_3O_9N$.

Table S9 Crystallographic data of $NaTi_2(PO_4)_3$ from the Rietveld refinement of 200 °C data (scan 168).

Formula		**Space group**		**Lattice parameters (Å)**		
$NaTi_2(PO_4)_3$		***R*-3*c* (# 167)**		**a = 8.4736(3) b = 21.9502(10)**		
Atom	Wyckoff symbol	*x*	*y*	*z*	Occ.	B_{iso} (Å^2)
Na	6b	0	0	0	1	4.35(14)
Ti	12c	0	0	0.1459 (1)	1	0.91(4)
P	18e	0.2857 (2)	0	0.25	1	1.15(5)
O1	36f	0.0307 (4)	0.2000 (4)	0.1926 (1)	1	1.62(8)
O2	36f	0.1934 (3)	0.1653 (3)	0.0900(1)	1	1.08 (7)